Mg-modified Zn-Co-Fe-La nano ferrites: A study of structural, morphological, vibrational, electro-optical, dielectric and magnetic evolution

M.I. Arshad [a,b,c,*], M.S. Hasan [d,**], Atta Ur Rehman [c], N. Amin [c], Le Duc Tung [a,b], N.T. Kim Thanh [a,b,*], N.A. Morley [e], Mongi Amami [f], Faisal Alresheedi [g], Safa Ezzine [f], M.A. Gadhi [h]

[a] Biophysics Group, Department of Physics and Astronomy, University College London, Gower Street, London WC1E 6BT, UK
[b] UCL Healthcare Biomagnetics and Nanomaterials Laboratories, 21 Albemarle Street, London W1S 4BS, UK
[c] Department of Physics, Govt. College University Faisalabad, 38000, Pakistan
[d] Department of Physics, The University of Lahore, Lahore 53700, Pakistan
[e] Department of Materials Science and Engineering, The University of Sheffield, S1 3JD, UK
[f] Department of Chemistry, College of Sciences, King Khalid University, Abha 61412, Saudi Arabia
[g] Department of Physics, College of Science, Qassim University, Buraidah 51452, Saudi Arabia
[h] Bahawalpur Institute of Nuclear Medicine and Oncology (BINO) Bahawalpur, Pakistan

ARTICLE INFO

ABSTRACT

The series of $Zn_{0.4}Co_{0.6-x}Mg_xFe_{1.9}La_{0.1}O_4$ (x = 0.0, 0.15, 0.30, 0.45, 0.6) nanoferrites prepared via co-precipitation technique. Scherrer and Williamson-Hall (W-H) methods were used to find the crystallite size (29.6–39.2 nm and 31.6–36.3 nm, respectively) and lattice constant was calculated (8.406–8.395 Å). Moreover, Fourier transform infrared (FTIR) spectroscopy revealed the existence of absorption bands along with functional groups. The vibrations of O^{2-} ions at the tetrahedral and octahedral sites were shown by the Raman five active modes. DC resistivity reduced in the range of 5.2961×10^8 Ω cm to 9.6453×10^7 Ω cm for x = 0.0 to x = 0.6, respectively. The maximum DC resistivity and activation energy (0.1035 eV) were obtained at the parent sample ($Zn_{0.4}Co_{0.6}Fe_{1.9}La_{0.1}O_4$). The optical bandgaps reduced from 2.61 to 1.47 eV, as the Mg^{2+} contents increased. With increasing frequency the dielectric loss and the dielectric constant decrease. The magnetic parameters such as saturation magnetization (M_s = 60.82–25.94 emu/g), remnant magnetization (M_r = 47.82–18.64 emu/g), and coercivity (H_c = 1334–511 Oe) demonstrated reducing trends with the increase of Mg^{2+} doping. The best magnetic behavior of the as-prepared samples suitable in microwave devices was observed for $Zn_{0.4}Co_{0.6}Fe_{1.9}La_{0.1}O_4$ sample.

1. Introduction

The spinel ferrites are applicable in numerous fields due to their different properties. Nano-sized ferrite particles often exhibit unique and size-dependent properties compared to their bulk counterparts. These properties can include enhanced magnetic properties, improved electrical conductivity, and altered optical properties. Nano ferrites offer an opportunity for fundamental research to explore the effects of quantum confinement, surface interactions, and size-induced phenomena on material properties. Investigation of size effects is of scientific interest and this research contributes to our understanding of materials at the nanoscale. Nano-sized ferrites can undergo changes in crystal structure or lattice parameters, affecting their magnetic and electrical behavior. The high surface area in nano ferrites can lead to increased surface energy, which can influence the material's reactivity, stability, and surface magnetic properties. Nano-sized ferrite particles sometimes exhibit higher magnetization values compared to their bulk counterparts due to a higher surface-to-volume ratio. Coercivity, which is the resistance of a material to demagnetization, can be enhanced in nano ferrites, making them useful for applications like high-density magnetic

Table 1
The stoichiometric ratios in grams used in the synthesis of Mg doped $Zn_{0.4}Co_{0.6-x}Fe_{1.9}La_{0.1}O_4$ (ZCL) ferrites.

X	Composition	$Zn_{0.4}$	$Co_{0.6-x}$	Mg_x	$Fe_{1.9}$	$La_{0.1}$
0.00	$Zn_{0.4}Co_{0.6}Fe_{1.9}La_{0.1}O_4$	1.189	1.746	0.0	7.676	0.433
0.15	$Zn_{0.4}Co_{0.45}Mg_{0.15}Fe_{1.9}La_{0.1}O_4$	1.189	1.309	0.385	7.676	0.433
0.30	$Zn_{0.4}Co_{0.30}Mg_{0.30}Fe_{1.9}La_{0.1}O_4$	1.189	0.873	0.769	7.676	0.433
0.45	$Zn_{0.4}Co_{0.15}Mg_{0.45}Fe_{1.9}La_{0.1}O_4$	1.189	0.436	1.154	7.676	0.433
0.60	$Zn_{0.4}Mg_{0.60}Fe_{1.9}La_{0.1}O_4$	1.189	0.0	1.538	7.676	0.433
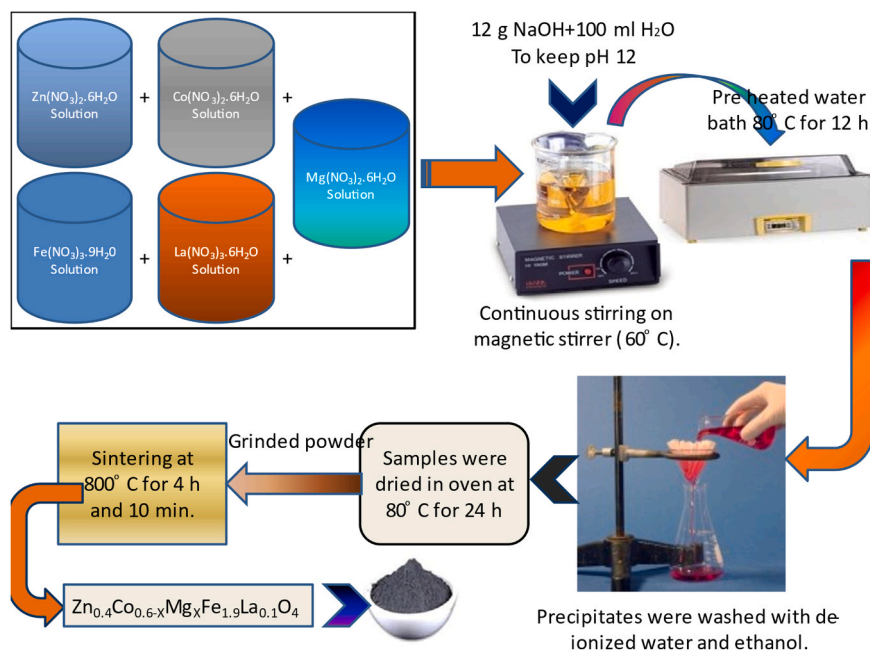
Fig. 1. Schematic diagram of Mg^{2+} doped ZCL spinel nano ferrites.

recording. Such characteristics of spinel nano ferrites are associated to preparation route and processing conditions for magnetic stability, homogenous size and the shape of the nano ferrite [1]. AB_2O_4 is the universal formula for spinel ferrites where *A* is divalent cations, and *B* trivalent cations [2]. Spinel ferrite demonstrates high resistivity, low eddy current losses and high permeability [3]. By controlling the size and shape of nano ferrite particles, we can tailor their properties to meet specific application requirements. Such characteristics of spinel ferrites lead to be applicable in different fields including biomedicine [4], magnetic resonance imaging (MRI) [5], memory storage gadgets [6], microwave absorbance [7], antenna rods [8], microwave devices [9], drug delivery [10], and power transformers [11].

Different synthetic techniques including spray pyrolysis [12], the hydrothermal technique [13], refluxing microwave method [14], the self-igniting process [15,16] and the co-precipitation route [17,18] were used to synthesize the nano ferrite powder. Co-precipitation process is simple and economical for preparation of nanoparticles as compared to others [18]. Co-precipitation can be conducted using environmentally friendly reagents and conditions, aligning with principles of green chemistry, which promote sustainable and eco-friendly practices in chemical processes. Moreover, this synthetic method offers benefits in terms of regulating particle size, achieving molecular homogeneity, and facilitating swift reactions [19–21].

Thomas *et al.,* prepared the Mg^{2+} inserted Co^{2+} soft ferrites by the application of solution combustion process. The maximum crystallite size (*D*) was 113 nm at *x* = 0.2. Saturation magnetization (56–34 emu^{-1}) and coercivity (930–89 Oe) were reduced with the increment of Mg^{2+} [16]. Mammo *et al.,* determined the effects of Mg^{2+} inserted Co^{2+} nano-ferrites fabricated by sol-gel auto combustion process. The DC resistivity increased up to 10^7 Ω.cm and saturation magnetization

decreased with Mg^{2+} doping and recommended the nano-particles for higher-frequency electronic devices [15]. Bhukal *et al.,* synthesized the Mg-doped Zn–Co nano composites by sol-gel auto combustion procedure and observed the electrical resistivity up to 10^9 Ω.cm. With the increase of Mg^{2+} insertion the saturation magnetization decreased from 55.13 to 24.17 emu/g [22]. Lodhi *et al.,* developed the $MgCo_xZn_{1-x}Fe_2O_4$ soft ferrites by employing a micro-emulsion route and stated the reduction in crystallite size and lattice constant with the addition of magnesium. The optimized magnetic properties of sample with *x* = 0.5 suggests the use in high-density recording media [23]. Rafiq *et al.,* prepared Mg–Zn nano-crystals with Co^{2+} doping by co-precipitation route and found that the lattice constant decreased with doping of Co^{2+}. The minimum coercivity was observed at *x* = 0.15 [24]. Liu *et al.,* synthesized the $Ni_{0.5}Zn_{0.4}Mg_{0.1}La_{0.1}Fe_{1.99}O_4$ nano ferrite by self-igniting process and reported the grain size of 26 nm. The as-prepared materials were annealed at 1023 K and suggested that Mg-La doped Ni-Zn sample applicable in electromagnetic wave attenuation [25]. Gaba *et al.* studied the physical properties of $MgLa_xFe_{2-x}O_4$ ferrites for microwave absorption applications. The extreme coercivity (H_c = 30.59 Oe) and saturation magnetization (M_S = 19.39 emug^{-1}) were noticed at *x* = 0.05 [26]. Thomas Dippong *et al.* synthesized the SiO_2 inserted Co ferrites and found the reduction in crystallite size with the addition of silica matrix [27]. They also observed the effect of Co/Fe ratio on oxide nanoparticles and found the crystallite size less than 100 nm [19]. Paul Barvinschi *et al.* prepared the cobalt ferrite-SiO_2 nanocomposites and found the crystallite size in the range of 3–10 nm [28]. Thomas Dippong *et al.* investigated the sono-photocatalytic activity SiO_2 embedded Mn-Zn ferrites [29].

This research investigates how the introduction of magnesium ions affects the structural, morphological, vibrational, electro-optical, dielectric, and magnetic properties of these ferrites. Notably, the
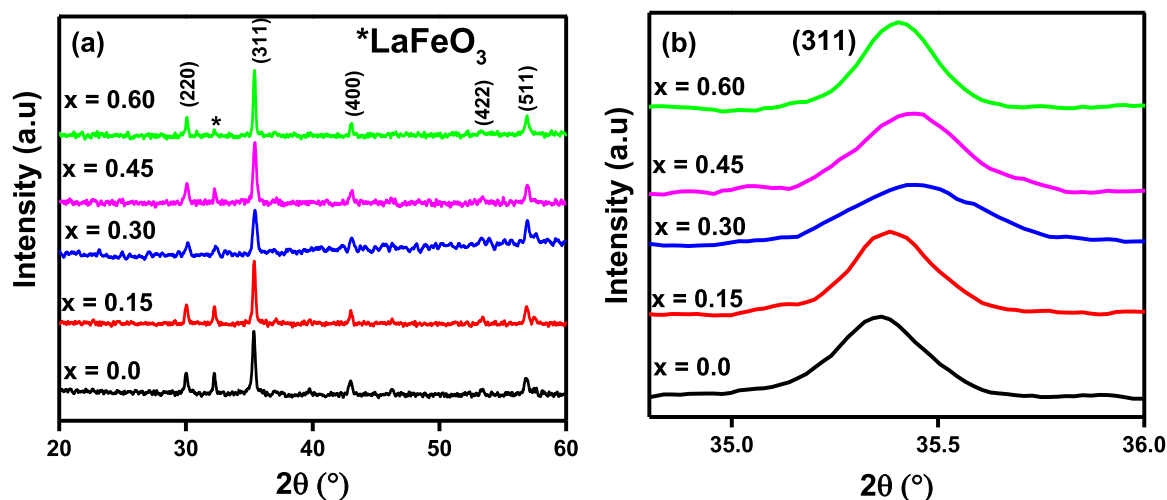
Fig. 2. (a-b): Bragg's angle (2θ)vs intensity for of Mg^{2+} doped ZCL nanoferrite powder **(a)** XRD spectra **(b)** Peak (311) shift spectra for Mg^{2+} ZCL nano ferrites.

Table 2

Concentration, peak position ($2\theta hkl$ – 311), d-spacing, the crystallite size (D), unit cell volume (V), the lattice constant (a_{exp}, a_{th}), experimental lattice constant (a_o) using Nelson Riley function F(θ), X-ray, bulk, relative density (d_x, d_B, d_R) and porosity percentage P (%) of Mg^{2+} doped ZCL nano ferrites.

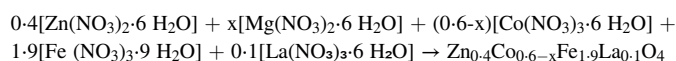| Concentration (x)		0.0	0.15	0.3	0.45	0.6
2θ (*hkl*-311) (Degree)		35.3569	35.3898	35.4486	35.4343	35.4044
d-spacing		2.5346	2.5323	2.5282	2.5292	2.5313
$D\pm0.1$ (nm)	Scherrer's formula	29.6	26.5	24.8	27.8	39.2
	W-H method	31.6	27.8	23.8	29.5	36.3
Strain using W-H method (ε)		-1.1935×10^{-4}	0.001	0.02471	-5.8332×10^{-5}	-3.3268×10^{-4}
a_{exp} (Å) (±0.0004)		8.4063	8.3988	8.3853	8.3886	8.3954
V (Å)^3		594.05	592.45	589.60	590.29	591.74
a_o(Å) using F(θ) function		8.3938	8.3907	8.3637	8.3884	8.3904
d_x (gcm^{-3})		5.48	5.38	5.29	5.17	5.04
d_B (gcm^{-3})		4.14	4.06	3.97	3.88	3.79
d_R(%)		132.53	132.65	133.41	133.37	133.17
P (%)		24.54	24.61	25.04	25.022	24.91
S (cm^2/g)		36.89	42.11	45.51	41.63	30.31
P		116.93	104.45	98.43	110.09	154.92
γ_P (Å)		0.7528	0.7521	0.7509	0.7512	0.7518
L_A (Å)		3.6399	3.6366	3.6308	3.6322	3.6352
L_B (Å)		2.9716	2.9689	2.9642	2.9653	2.9677

material exhibits decreased resistivity, reduced optical band gap energy and magnetization. These findings suggest improved conductivity and reduced microwave absorption, making it promising for efficient microwave device applications, such as waveguides and antennas. This research contributes to advancing microwave technology by harnessing the unique characteristics of Mg-modified ferrites.

In our work, the Mg^{2+} doped zinc-cobalt-lanthanite (ZCL) nano ferrites with compositional formula $Zn_{0.4}Co_{0.6-x}Mg_xFe_{1.9}La_{0.1}O_4$ (x = 0.0, 0.15, 0.3, 0.45, 0.6) were developed by co-precipitation procedure. Here, Zn-Co-La nano ferrite was chosen from among numerous spinel ferrites due to its tailored properties, potential for enhanced performance, and existing research literature highlighting its effectiveness in similar applications. Its availability, research gap-filling potential, and specific advantages in niche areas also played a role in this selection, aligning with the research objectives and making it a practical and promising candidate for the study. The ZCL nanoferrites are specially synthesized for their microwave applications. The structural, morphological, vibrational, electro-optical, dielectric and magnetic characteristics of nano ferrite samples were determined.

2. Experimental

2.1. Synthesis process

Mg^{2+} substituted $Zn_{0.4}Co_{0.6-x}Fe_{1.9}La_{0.1}O_4$ (x = 0.0, 0.15, 0.3, 0.45, 0.6) powder were prepared by co-precipitation process. 99.9% pure Sigma-Aldrich salts including zinc nitrate [Zn(NO$_3$)$_2$.6 H$_2$O], magnesium nitrate [Mg(NO$_3$)$_2$.6 H$_2$O], cobalt nitrate [Co(NO$_3$)$_2$.6 H$_2$O], iron nitrate [Fe (NO$_3$)$_3$.9 H$_2$O] and lanthanum nitrate [La(NO$_3$)$_3$.6 H$_2$O] were used. The weights given in Table 1, with the help of Ja1003c 0.001 g Internal Calibration Digital Electronic Analytical Balance of Zn, Mg, Co, Fe and La nitrates were inserted in deionized water according to the stoichiometric ratios. At 60 °C, the solutions were mixed with continuous stirring (78-I magnetic stirrer). NaOH solution was inserted as a precipitous factor to retain pH 12. The following chemical reaction appeared for the formation of nanoferrites:

$0.4[Zn(NO_3)_2 \cdot 6 \ H_2O] + x[Mg(NO_3)_2 \cdot 6 \ H_2O] + (0.6-x)[Co(NO_3)_3 \cdot 6 \ H_2O] + 1.9[Fe \ (NO_3)_3 \cdot 9 \ H_2O] + 0.1[La(NO_3)_3 \cdot 6 \ H_2O] \rightarrow Zn_{0.4}Co_{0.6-x}Fe_{1.9}La_{0.1}O_4$

They were kept in 80 °C pre-heated water (Kambic water bath) for 12 hrs. To remove impurities from precipitates the solutions were cleaned with deionized water and ethanol by the support of filter papers. Then the particles were dried in an oven (Biotechnologies inc. oven) at 80 °C. The obtained materials were grind into powder by using granite mortar
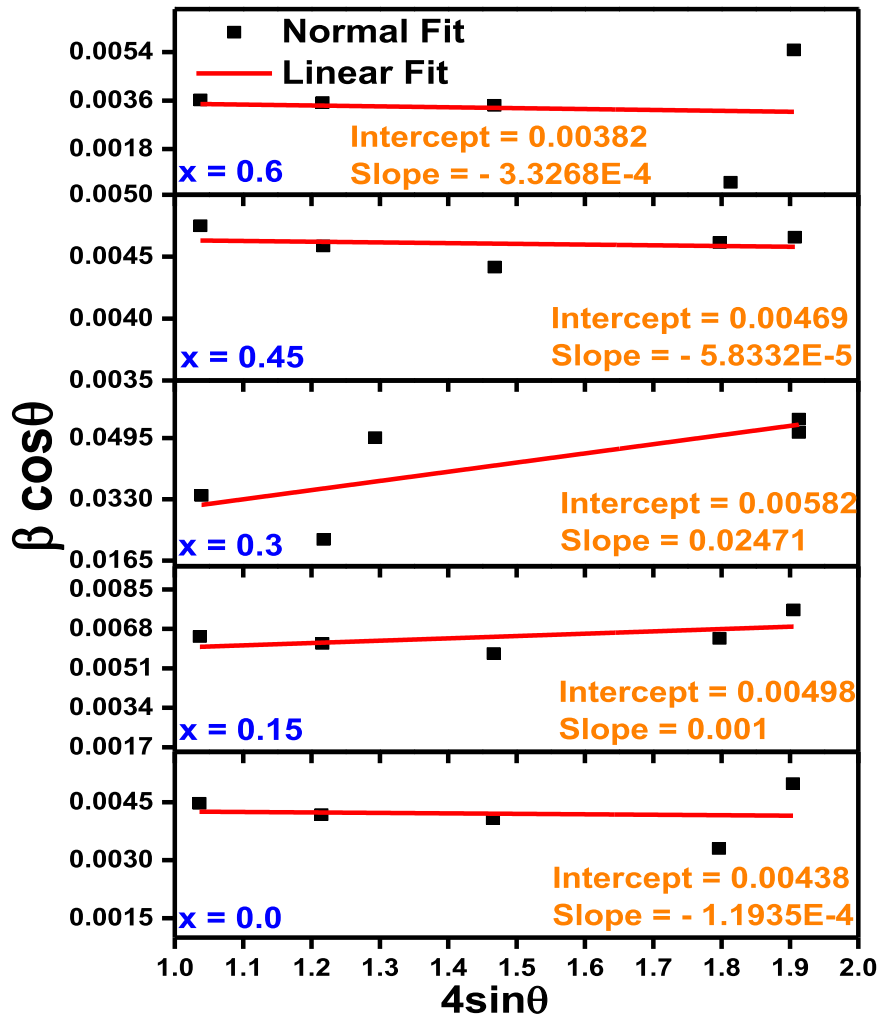
Fig. 3. W-H plot for Mg^{2+} doped ZCL powder.

pestle. The obtained samples were sintered (DM-12 N Dming Technology Muffle furnace) at 800 °C for 4 hrs and 10 min and following the grounding for fine powder. The schematic diagram of preparation powder is given in Fig. 1.

2.2. Characterization techniques

The spinel cubic structures in nanoferrite samples were confirmed by X-ray Diffraction (Bruker D8) where Cu-K_α is source with $\lambda = 1.5406$ Å. Morphology of nano-ferrites was studied with Scanning Electron Microscopy (SEM). Two probes I-V system with Keithley 2401 was employed to investigate electrical properties. Ultraviolet-visible (UV–vis) photometer was utilized to study the optical bandgap energy. FTIR spectroscopy (Perkin) was used to investigate the absorption bands within the 400–3500 cm^{-1} frequency range. Raman spectroscopy was applied to determine vibrational properties. Dielectric parameters were investigated through LCR meter. Vibrating Sample Magnetometer (VSM) was employed to study the magnetic nature of fabricated nano-composites with the application of magnetic field up to 1.5 T.

3. Results and discussions

3.1. Structural study

X-ray diffraction patterns for of Mg^{2+} doped ZCL nanoferrites are presented in Fig. 2(a-b). The prominent peaks specified with (220),

(311), (400), (422), and (511) confirmed the spinel structure of as-prepared nano ferrites (space group; F d-3 m) [30] and peak marked with symbol (*) belongs to orthorhombic configuration $LaFeO_3$ (space group; P b n m) [31,32]. Volume of $LaFeO_3$ was decreased with the substitution of Mg^{2+}. It can be seen from Fig. 2(b) peak (311) shifts towards larger angle up to $x = 0.3$ and for $x = 0.45$–0.6 towards smaller angle compared to x = 0.3. The shift towards smaller angles for x = 0.45–0.6 implies a decrease in lattice spacing. This suggests that as the concentration of Mg^{2+} ions increases in this range, their smaller ionic radius (0.71 Å) [33] replaced the Co^{+2} having larger ionic radius (0.82 Å , 0.74 Å) [34] closer together, resulting in a reduction of the crystal lattice spacing.

The Bragg's angle for peak (311) and d-spacing (d) calculated using Bragg's law [35] are reported in Table 2. For crystallite size (D), Scherrer's formula was applied [36]. The crystallite size has lowest value of 24.88 nm at $x = 0.3$ (Table 2). Mg^{2+} ions have a smaller ionic radius compared to Co^{2+} ions. When Mg^{2+} ions are substituted for Co^{2+} ions in the crystal lattice, the smaller size of Mg^{2+} ions allows them to occupy the lattice sites more closely together. This leads to a more compact crystal structure with smaller crystallites. The increase in particle aggregation with higher magnesium ion content in the prepared samples can be attributed to the smaller ionic radius of magnesium ions compared to the host ions in the material. When magnesium ions are introduced in greater quantities, they can occupy spaces within the crystal lattice that would normally be filled by larger host ions. This disrupts the regular crystal structure, leading to increased particle
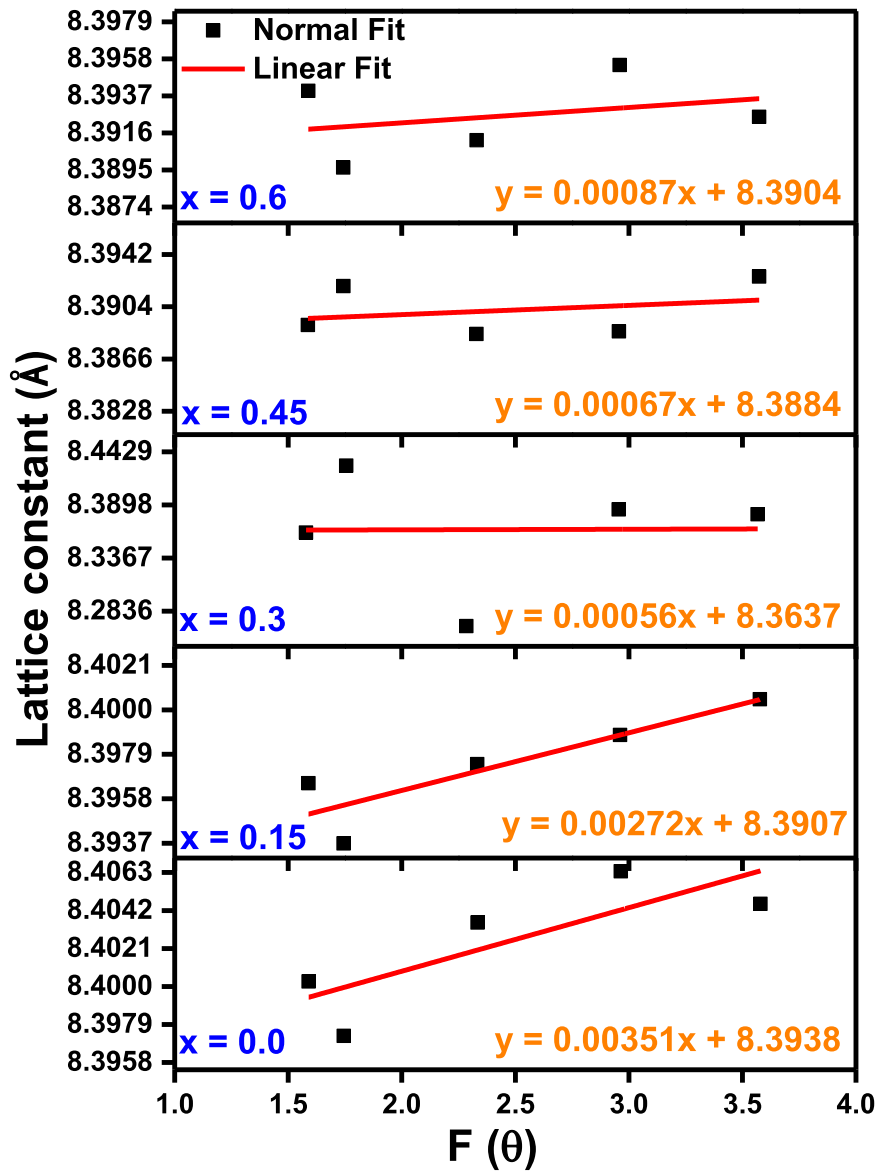
Fig. 4. Nelson Riley function F(θ) plots for Mg^{2+} doped ZCL samples.

Table 3
Cationic arrangement at sub-lattice *A* and *B* sites of Mg^{2+} doped ZCL nano ferrites.

x	Tetrahedral site (*A*)	Octahedral site [*B*]
0.0	(Zn$_{0.4}$Co$_{0.06}$Fe$_{0.54}$)	[Co$_{0.54}$Fe$_{1.36}$La$_{0.1}$] O$_4$
0.15	(Zn$_{0.4}$Co$_{0.045}$Mg$_{0.0675}$Fe$_{0.4875}$)	[Co$_{0.405}$Mg$_{0.0825}$Fe$_{1.4125}$La$_{0.1}$]O$_4$
0.3	(Zn$_{0.4}$Co$_{0.03}$Mg$_{0.135}$Fe$_{0.435}$)	[Co$_{0.27}$Mg$_{0.165}$Fe$_{1.465}$La$_{0.1}$]O$_4$
0.45	(Zn$_{0.4}$Co$_{0.015}$Mg$_{0.2025}$Fe$_{0.3825}$)	[Co$_{0.135}$Mg$_{0.2475}$Fe$_{1.5175}$La$_{0.1}$]O$_4$
0.6	(Zn$_{0.4}$Mg$_{0.27}$Fe$_{0.33}$)	[Mg$_{0.33}$Fe$_{1.57}$La$_{0.1}$]O$_4$

Table 4
Tetrahedral and octahedral ionic radii (r_A and r_B), the theoretical lattice constant (a_{th}), oxygen positional parameter (*U*) and tolerance factor (*T*) for Mg^{2+} doped ZCL nano ferrites.

x	r_A (Å)	r_B (Å)	a_{th} (Å)	U (Å)	T
0.00	0.5954	0.6914	8.3126	0.3830	1.0371
0.15	0.5999	0.6877	8.3097	0.3833	1.0382
0.30	0.6035	0.6847	8.3072	0.3836	1.0392
0.45	0.6075	0.6814	8.3046	0.3840	1.0403
0.60	0.6116	0.6781	8.3021	0.3843	1.0413

aggregation as the lattice becomes more compact. Essentially, the smaller magnesium ions create a tighter packing of particles, resulting in larger aggregations within the material. Previously, M. S. Hasan *et al.* found the crystallite size showing the similar trend for Mg and La co-doped ferrites [17]. Scherrer formula only describes the consequence of crystallite size on broadening of peaks and do not enlighten the production of straining during crystal evolution because of point effect and rain boundary. In order to explain this factor Williamson-Hall (W-H) method is applied which states that the peak broadening is addition of size and strain. So, $\beta = \beta_{size} + \beta_{strain}$. Therefore, $\beta = \frac{0.9\lambda}{D} \times \frac{1}{\cos\theta} + 4\varepsilon\tan\theta$.

On rearranging the equation, we get; $\beta\cos\theta = \varepsilon(4\sin\theta) + \frac{0.9\lambda}{D}$. Fig. 3 is the W-H plots with 4sinθ versus βcosθ indicating the XRD peak for Mg^{2+} substituted ZCL nanoferrites. The average crystallite is determined by straight line interception and lattice strain created during crystal growth is calculated by slope. In the crystal matrix the strain is based on lattice narrowing or extension corresponding to size than bulk [37]. Table 2 illustrates the average crystallite obtained through W-H plot. 23.81 nm (*x* = 0.3) is the lowest calculated average crystallite size value obtained from W-H method as illustrated in Table 2. Furthermore, the lattice

Table 5

Bond lengths (R_A, R_B), bond edge lengths (d_{AL}, d_{BL}, and d_{BLU}) for Mg^{2+} doped ZCL nano ferrites.

x	Bond lengths (Å)		Bond edge lengths (Å)		
	R_A	R_B	d_{AL}	d_{BL}	d_{BLU}
0.00	1.9369	2.0341	3.1631	2.7811	2.9751
0.15	1.9404	2.0292	3.1687	2.7701	2.9727
0.30	1.9415	2.0235	3.1705	2.7587	2.9682
0.45	1.9469	2.0216	3.1794	2.7522	2.9696
0.60	1.9532	2.0205	3.1897	2.7467	2.9723

Table 6

Values of inter-ionic lengths among Me–Me and Me–O for Mg^{2+} doped ZCL nano ferrites.

x	Cation – Anion (Me – O)				Cation – Cation (Me – Me)				
	p (Å)	q (Å)	r (Å)	s (Å)	b (Å)	c (Å)	d (Å)	e (Å)	f (Å)
0.00	2.0341	1.9369	3.7090	3.6790	2.9720	3.4851	3.6400	5.4600	5.1477
0.15	2.0292	1.9404	3.7157	3.6774	2.9694	3.4819	3.6367	5.4551	5.1431
0.30	2.0235	1.9415	3.7178	3.6729	2.9646	3.4763	3.6309	5.4464	5.1349
0.45	2.0216	1.9469	3.7281	3.6759	2.9658	3.4777	3.6323	5.4485	5.1369
0.60	2.0205	1.9532	3.7402	3.6805	2.9682	3.4805	3.6353	5.4529	5.1411

strain showed maximum value for $x = 0.3$ obtained from W-H plot.

The experimental lattice constant (a_{exp}) [38] was calculated and reported in Table 2. It can be seen that, for $x = 0.3$, the experimental lattice constant (a_{exp}) was minimum. The dissimilarities in lattice constants are associated to the difference in ionic radii of Mg^{2+} (0.72 Å) and Co^{2+} (0.74 Å) and peak shifts with the dopant concentration (Fig. 2(b)). The introduction of Mg^{2+} ions disrupts the regular crystal lattice, causing lattice distortion. This distortion can result in smaller crystallites as it becomes energetically favorable for the crystal to form smaller

Table 7

Bond angles for Mg^{2+} doped Zn-Co-La soft ferrites.

x	θ_1	θ_2	θ_3	θ_4	θ_5
0.00	122.69	142.17	93.86	126.14	72.75
0.15	122.58	141.70	94.05	126.18	72.46
0.30	122.49	141.32	94.20	126.21	72.22
0.45	122.38	140.91	94.36	126.24	71.95
0.60	122.28	140.49	94.53	126.28	71.69

domains with fewer lattice defects. Also, the decrease in lattice constant with an increase in Mg concentration and a decrease in Co concentration can be explained by the fact that Mg ions have a smaller ionic radius compared to Co ions. The true value of experimental lattice constant (a_o) determined by using Nelson Riley Function $F(\theta)$ plots (Fig. 4) for each reflection constructing a linear regression. In Fig. 4, we extrapolate linear line to $F(\theta) = 0$ or 90°. The calculated true values experimental lattice constant (a_o) from the y-intercept of extrapolation function $F(\theta)$ are reported in Table 2. The volume of unit cell ($V = a^3$) [39] has a minimum at $x = 0.3$. The X-ray and bulk densities (d_x and d_B) [40] were (listed in Table 2). The fact that the values of d_x are larger than those of d_B is due to the uncommon empty spaces occurrence through the preparation and annealing in nano ferrites [41]. Furthermore, d_x and d_B decreased with Mg^{2+} doping (Table 2) and the relative density percentage ($d_R = d_X/d_B$) [42] increases from 132.53% to 133.41% for $x = 0.0–0.3$ and then reduced for $x = 0.45–0.6$. The porosity percentage [41] was determined and it has extreme result at $x = 0.3$. Different factors were calculated, like specific surface area (S) [43] and the packing factor (p) [41]. The values for "S" enhance up to $x = 0.3$ with
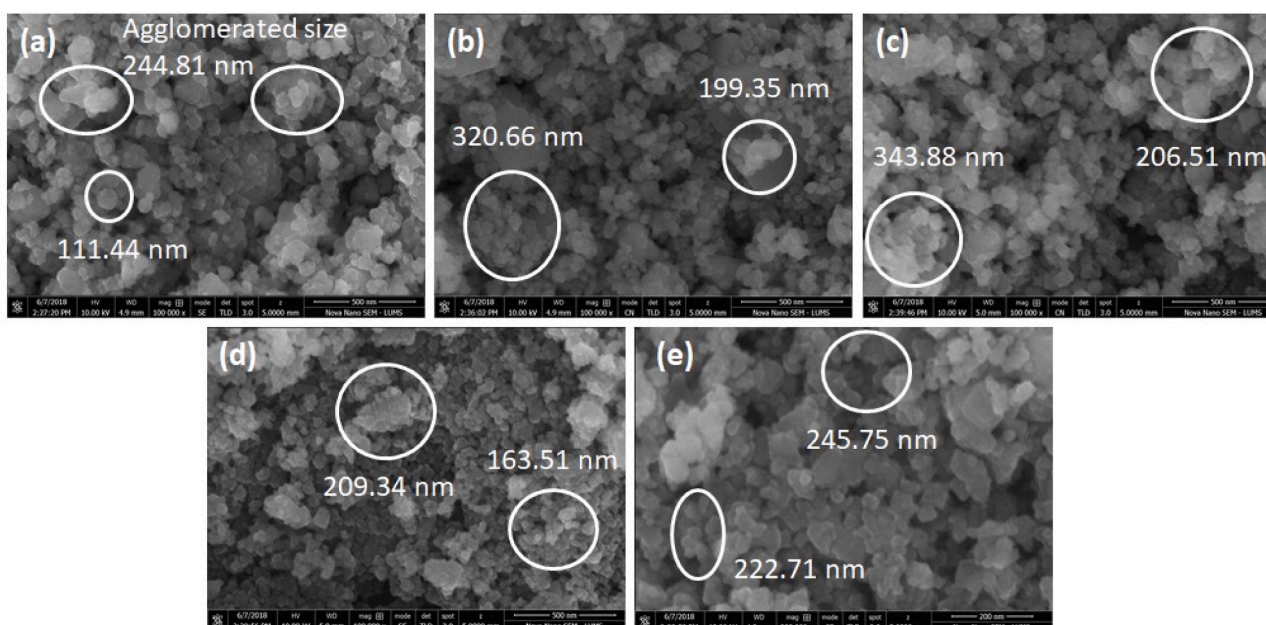
Fig. 5. (a-e): Micrographs for Mg^{2+} doped ZCL nano ferrites.
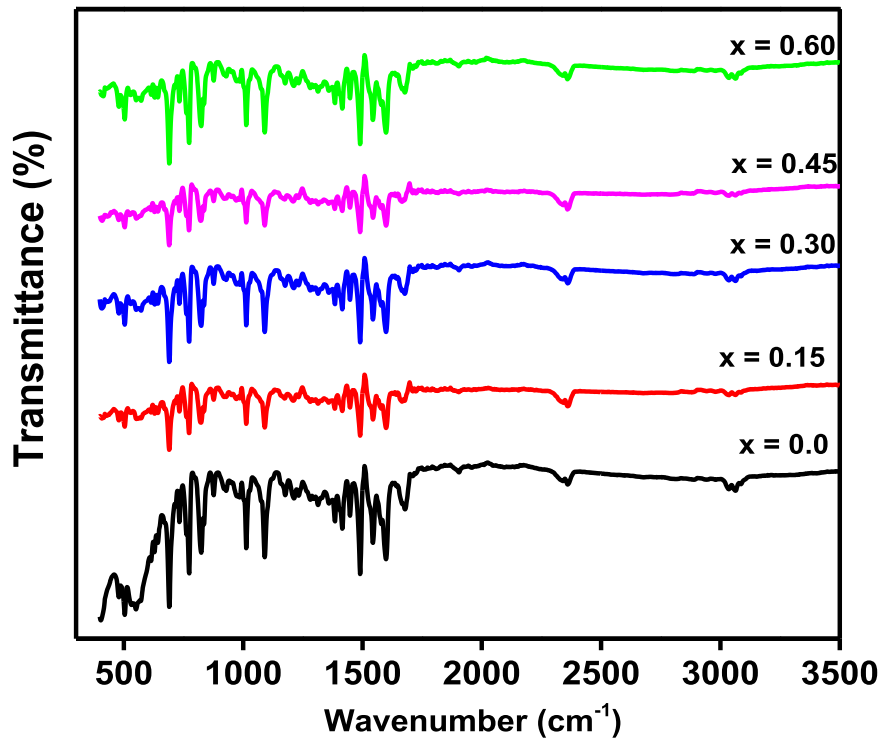
Fig. 6. FTIR spectra for Mg^{2+} doped ZCLnano ferrites.

Table 8
Absorption band positions and their respective intensities and force constants.

x	V_1 (cm^{-1})	I_1 (%)	K_Tx10^5 dyne. cm^{-1}	V_2 (cm^{-1})	I_2 (%)	K_Ox10^5 dyne. cm^{-1}
0.00	550.96	0.90618	2.22	413.57	0.91342	1.25
0.15	552.39	0.93892	2.23	409.28	0.93511	1.22
0.30	552.39	0.89983	2.23	407.85	0.90239	1.21
0.45	552.39	0.93451	2.23	406.42	0.93615	1.20
0.60	550.96	0.70348	2.22	403.56	0.68339	1.19

the addition of Mg^{2+} cations and then decrease. It was observed in Table 2 that the factor "*p*" has a lowest outcomes of 98.43 at $x = 0.3$. The dissimilarities in the cationic radii of Mg^{2+} and Co^{2+} cations is responsible of such behavior.

Hopping distances/lengths L_A and L_B for sub-lattice sites tetrahedral (*A*) and octahedral (*B*) between magnetic ions may cause the conductivity to increase. Table 2 showed the decrease in hopping length upto $x = 0.3$ and a small energy is essential to transfer charges amongst the cationic sites. The variation in hopping length may be due to differences in the radii of Mg^{2+} and Co^{2+} [44]. The polaron radius (γ_p) can also verify it. The values of the polaron radius (γ_p) for Mg^{2+} doped ZCL soft ferrites are given in Table 2. Reduction in the polaron radius reveals that a smaller energy is vital to transport charge carries between the cationic sites, and enhancement in values mean larger energy is needed for this purpose [45].

Tetrahedral (*A*) ionic radii (r_A) and octahedral (*B*) ionic radii (r_B) depend on cations distribution. Zn^{2+} occupies the tetrahedral *A*-site with normal spinel structure [46]. Co^{2+}, Mg^{2+} and Fe^{3+} cations reside both A and B sites [47,48]. Below equations are applied to investigate ionic radii r_A and r_B for tetrahedral and octahedral sites and most suitable cations distributions are demonstrated in Table 3.

$$r_A = [C_{AZn}.r(Zn^{2+}) + C_{ACo}.r(Co^{2+}) + C_{AMg}.r(Mg^{2+}) + C_{AFe}.r(Fe^{3+})]$$

$$r_B = \frac{1}{2}[C_{BCo}.r(Co^{2+}) + C_{BMg}.r(Mg^{2+}) + C_{BFe}.r(Fe^{3+}) + C_{BLa}.r(La^{3+})]O_4$$

In above relations C and r are fractional concentrations and ionic radii respectively Zn^{2+} (0.74 $A°$), Co^{2+} (0.74 $A°$), Mg^{2+} (0.72 $A°$), Fe^{3+} (0.64 $A°$) and La^{3+} (1.06 $A°$), respectively. C_{AZn}, C_{ACo}, C_{AMg} and C_{AFe} are associated to A-site concentrations and C_{BCo}, C_{BMg}, C_{BFe} and C_{BLa} B-site concentrations. Table 4 showed the ionic radii of Mg^{2+} inserted Zn-Co-La nanoferrites. It can be observed that r_A is amplified, and r_B decreases with the increase of Mg^{2+} doping for $x = 0.0 - 0.6$. The expansion in r_A is due to greater ionic radius of Co^{2+} (0.74 Å) contents that are substituted by lower ionic radius Mg^{2+} (0.72 Å). The reduction in r_B with the Mg^{2+} doping is because of shifting of Fe^{3+} (0.64 Å) from *B*-site to *A*-site. From the r_A and r_B, the theoretical lattice constant (a_{th}) [41] was found and listed in Table 4. The slight difference amongst "a_{th}" and "a_{exp}" is due to variations in ionic radii, the normal arrangements of ions supposition in unit cell structure for theoretical calculations [49].

Tetrahedral sites are diminutive to provide accommodation with the metal ions and slightly shift the oxygen ions. Such shifting of O^{2-} ions is expressed as an oxygen positional parameter (*U*) and $U = 0.375$ Å for ideal spinel structure [41]. The calculated *U* of fabricated spinel ferrites deviates from the standard value. Displacing of anions from ideal situation lead to deformations in sublattices and caused the deviation in *U* [50]. The increasing trend of *U* with the rising contents of Mg^{2+} may be attributed to the growth in tetrahedral sub-lattice arrangements to accommodate smaller ionic radii Mg^{2+} in replacement of larger ionic radii Co^{2+}. The tolerance factor [$T = \frac{1}{\sqrt{3}}\left(\frac{r_A+R_o}{r_B+R_o}\right) + \frac{1}{\sqrt{2}}\left(\frac{R_o}{r_A+R_o}\right)$] was used to make sure that synthesized nanoparticles are free of defects as given in Table 4. For ideal ferrite structure, *T* is equal to unity [51]. The enhancement in measured values of T is approaching unity and stretches the nanoferrites free of contaminations. "*T*" is approximately approached to 1 for all fabricated nanoferrites and it is improved with the increasing Mg^{2+} cations.

Shortest distance at *A*-site cations and O^{2-} ions and *B* site cations and O^{2-} ions are called bond length (R_A) and (R_B), respectively [41]. Values of R_A and R_B are listed in Table 5 where inconstant trends are seen with
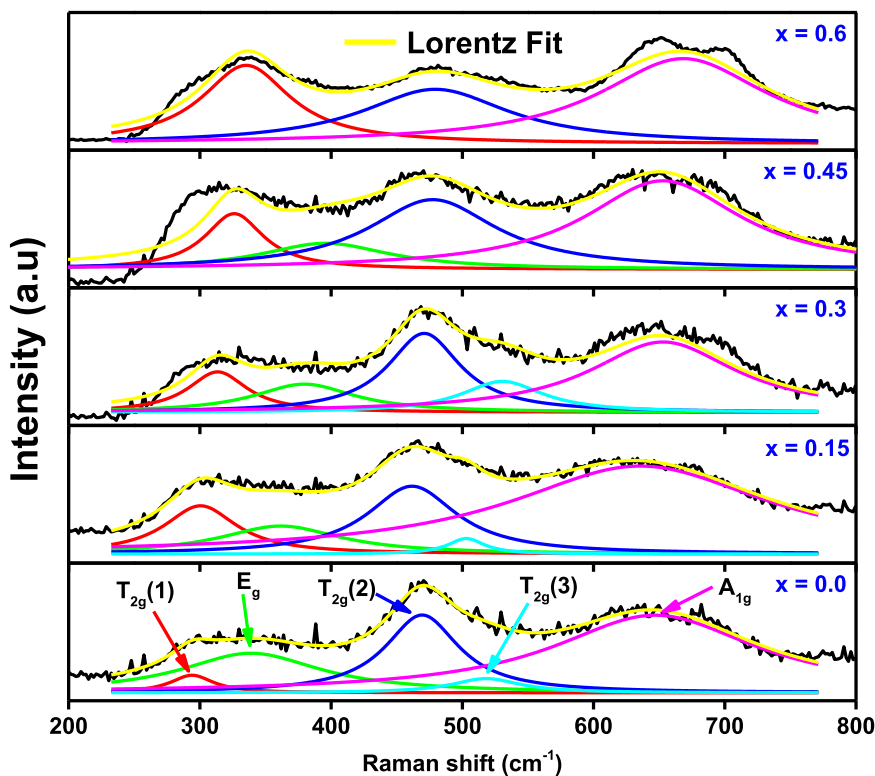
Fig. 7. A plot of Raman shift vs. intensity for Mg^{2+} doped ZCL nano ferrites.

Table 9
Raman modes for Mg^{2+} doped ZCL nano ferrites.

X	$T_{2g}(1)$	E_g	$T_{2g}(2)$	$T_{2g}(3)$	A_{1g}
0.00	236.19	327.11	388.15	472.23	636.75
0.15	294.03	338.91	469.33	518.21	646.81
0.30	313.51	379.60	470.93	530.45	652.74
0.45	326.16	395.89	477.43	—	652.91
0.60	335.29	—	479.39	—	668.36

the addition of Mg^{2+} ions. The Mg^{2+} (0.72 Å) ions shifted a large number of Fe^{3+} ions from the A to B site. Therefore, the values "r_A" of the A-site increase leading to an increase in tetrahedral bond length (R_A).

The inter-atomic lengths i.e., tetrahedral, shared octahedral, and unshared octahedral edge lengths are represented by d_{AL}, d_{BL}, and d_{BLU}, respectively. Distinctions in bond positions d_{AL}, d_{BL}, and d_{BLU} are linked to the allocation of metal ions in *A* and *B* lattice sites and are listed in Table 5. The expansion in ionic radii of r_A with the increasing concentration of Mg^{2+} is responsible for an increase in d_{AL}. On the other hand, a decrease in d_{BL} and d_{BLU} is because of contractions in ionic radii of r_B with the increase of Mg^{2+} contents [52].

Magnetic characteristics of soft-ferrites are associated to exchange forces as well as on the inter-ionic distance and bond angles between ions. *A–B*, *A–A* and *B–B* are the magnetic interactions associated to bond distance and angles between the ions. The bond angles and inter-ionic distances are directly and inversely proportional to strength of magnetic exchange forces [53]. The calculated inter-ionic lengths i.e., cations–anions (Me–O) and cations–cations (Me–Me) are given in Table 6.
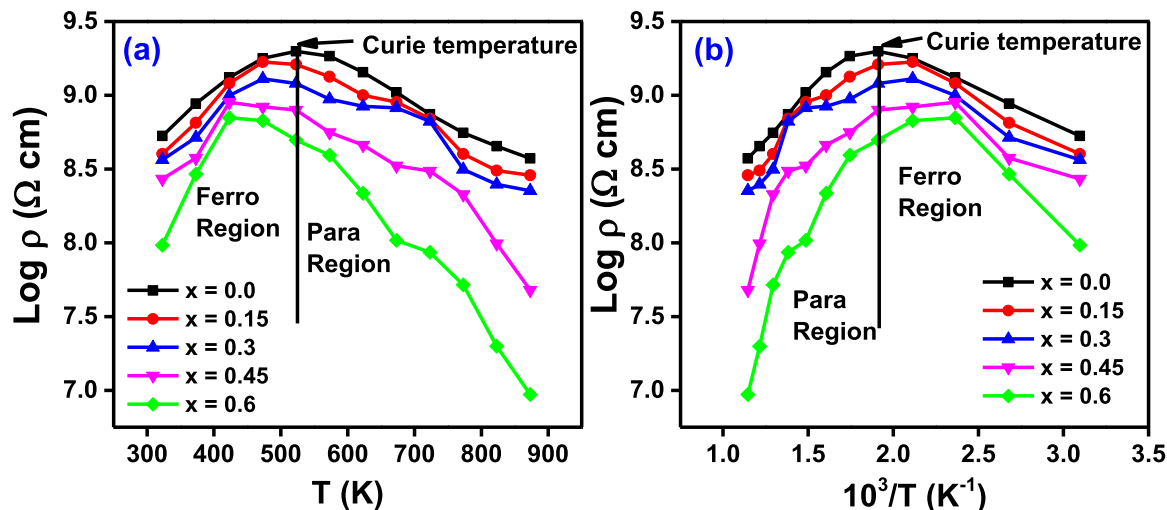
Fig. 8. (a-b): Resistivity versus temperature for Mg^{2+} doped ZCL nano ferrites (a) log ρ vs T plots (b) log ρ vs $10^3/T$ plots.

Table 10

Electrical parameters for Mg^{2+} doped ZCL nano ferrites.

x	0.00	0.15	0.30	0.45	0.60
$\rho(\Omega\,cm)$	5.2961×10^8	4.0037×10^8	3.6547×10^8	2.7124×10^8	9.6453×10^7
T_C (K)	522	471	468	425	420
E_p (eV)	0.2027	0.1704	0.1604	0.1610	0.1953
E_f (eV)	0.0992	0.1289	0.1359	0.1369	0.1738
$\Delta E = E_p - E_f$ (eV)	0.1035	0.0414	0.0245	0.0241	0.0215
μ_d ($cm^2 V^{-1} s^{-1}$)	2.0369×10^{-22}	2.6896×10^{-22}	2.9489×10^{-22}	3.9769×10^{-22}	1.1194×10^{-21}
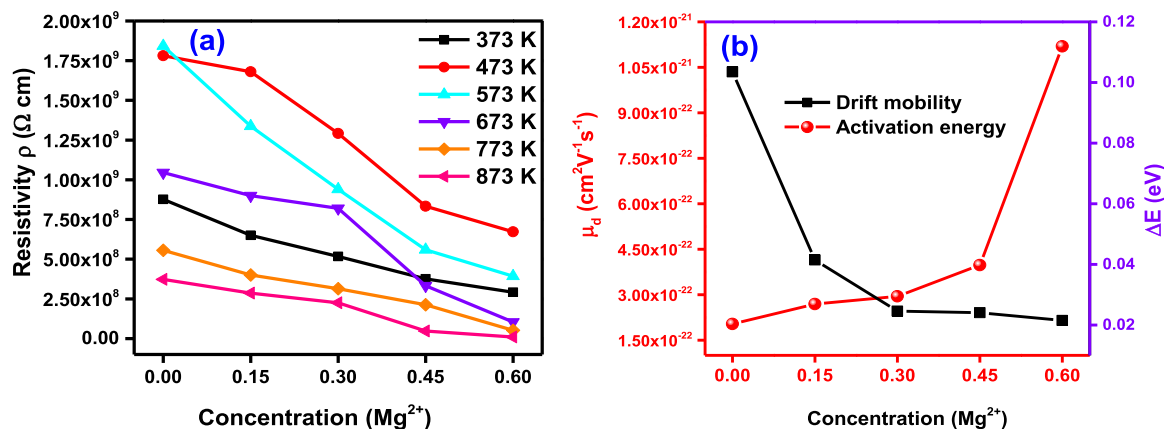
Fig. 9. (a-b): Plots of (a) Resistivity vs. concentration at different temperatures (b) Activation energy and drift mobility at 323 K for Mg^{2+} doped ZCL nano ferrites.
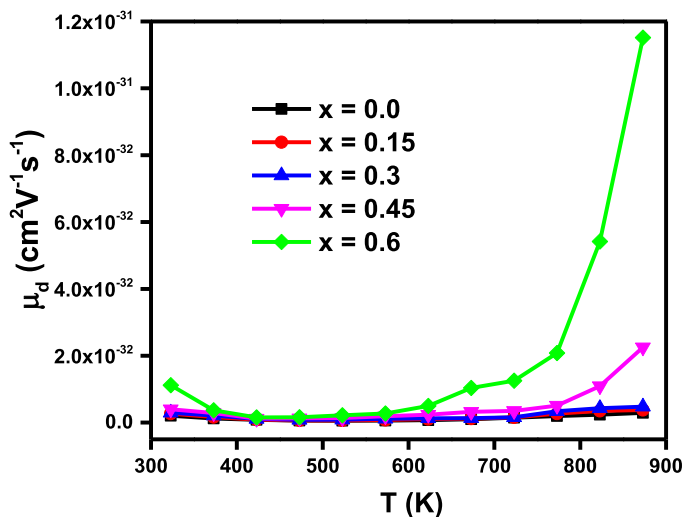
Fig. 10. The plots of drift mobility versus temperature of Mg^{2+} doped ZCLnano ferrites.

By the application of interionic distance, the bond angles were also computed [54]. Table 7 confirmed that by enhancing the Mg^{2+} concentration, the bond angles θ_1, θ_2, and θ_5 decreased and signified the weak (*A–B*) and (*A–A*) interactions. The increased in θ_2 and θ_4 bond angles confirmed the strong (*B–B*) interaction with insertion of Mg^{2+} [52].

3.2. Morphological study

Micro images obtained from Scanning electron microscopy (SEM) are given in Fig. 5(a-e). The micrographs (Fig. 5(a-e)) reveal that the nanoparticles have irregular shape. The accurate particle size is difficult to determine from micro images due to boundaries of particles being not clear. The observed agglomerated shapes are due to the loose packing of particles [26] and the agglomeration increases with Mg^{2+} doping. The sizes of agglomeration are in the order of few nanometers and being shown in Fig. 5(a-e). The different size of particles may be due to presence of some impurities. Similar shapes and agglomeration of nanoparticles were determined by Mohd. Hashim *et al.* for Co doped Mg-Zn ferrites [1].

3.3. FTIR study

Fig. 6 shows recorded FTIR spectra for Mg^{2+} doped ZCL within the frequency range from 400 to 3500 cm^{-1}. Two significant absorption bands [55], including high (γ_1) 550.96 cm^{-1} – 552.39 cm^{-1} and low (γ_2) 413.57 cm^{-1} – 403.56 cm^{-1}, are observed in this spectrum (Table 8) where, γ_1 and γ_2 are associated to tetrahedral and octahedral [56] complexes of metal oxide in the spinel matrix [49]. Previously, Santosh Bhukal e*t al.* determined the low frequency band in the range of 434 cm^{-1} for Mg substituted CoZn ferrites [22]. Within ZCL ferrite samples, we observed a nearly equal distribution of Fe^{3+} ions occupying both the tetrahedral A-site and the octahedral B-site, and this distribution extends to Mg^{2+} ions as well. This implies that both electrons and holes become available at the B-site due to the coexistence of Mg^{2+} and Fe^{3+} ions. Additionally, there is an inclination for La^{3+} ions to substitute Fe^{3+} ions within the octahedral B-sites. This behavior can be rationalized by considering variations in lattice constant values corresponding to different dopant ratios or by proposing their incorporation at interstitial sites within the structural framework [26]. Besides two major absorption peaks, additional peaks at different wavenumbers also observed. Absorption band around 840 cm^{-1} can be attributed to C-C, 2356 cm^{-1} to CO_2 and OH stretching vibrations [57,58]. Absorption peaks at 1109 cm^{-1}, 1360 cm^{-1}, and 1556 cm^{-1} are due to C-H, NO_3 group, and C=O antisymmetric stretching vibrations, respectively.
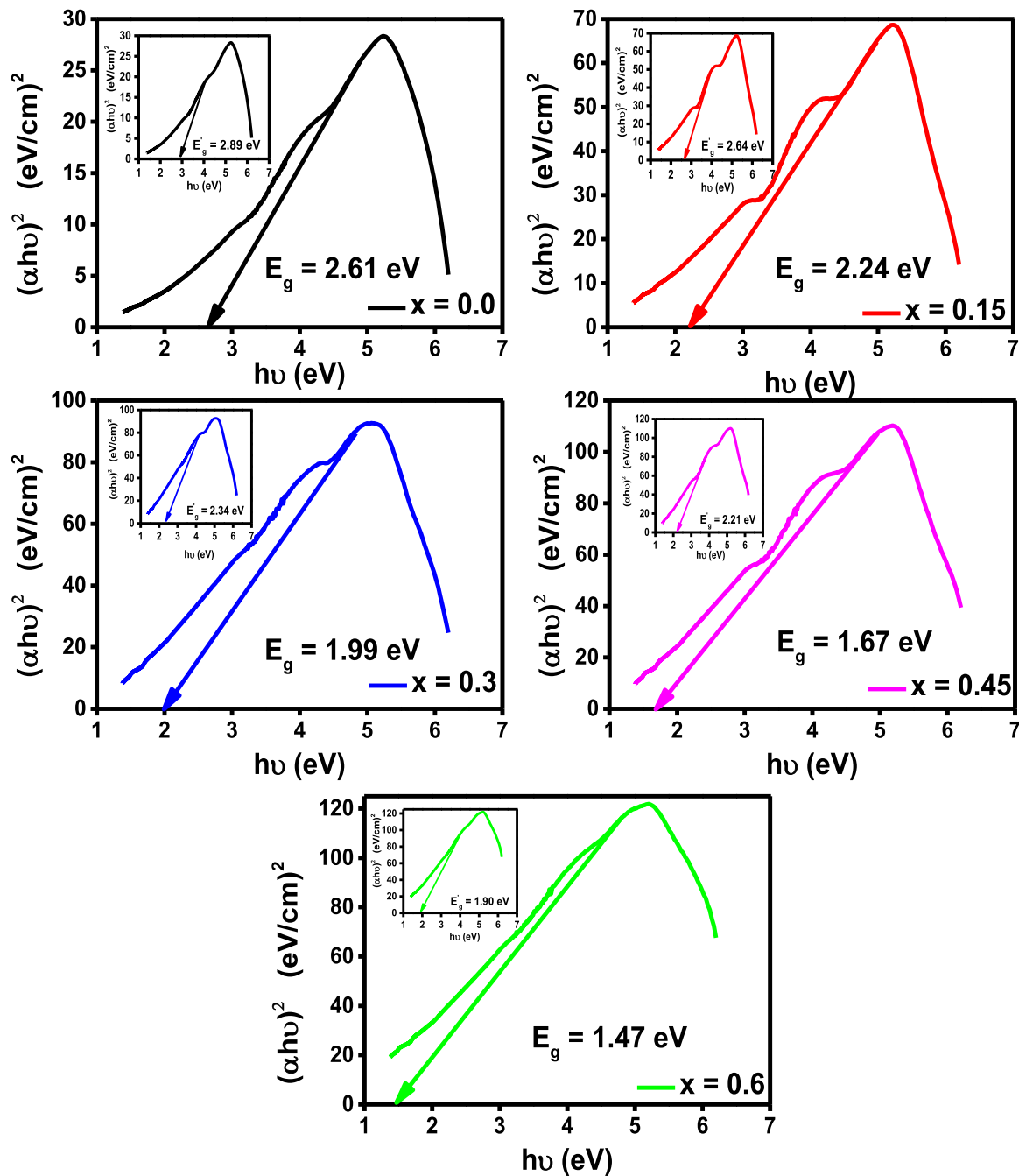
Fig. 11. Tauc plots for optical bandgap (E_g and E'_g) of Mg^{2+} doped ZCLnano ferritesnano ferrites.

3.4. Raman spectroscopy study

Fig. 7 shows recorded Raman spectra for Mg^{2+} doped Zn-Co-La nano ferrites. The group theory predict five active phonon Raman modes such as; $\Gamma = 1A_{1g} + 1E_g + 3T_{2g}$ for regular spinel structure of soft ferrites [59]. The presence of an inversion center in the Centro-symmetrical space group $Fd - 3m$ for similar vibrational modes, indicates the shared exclusion of Raman (R) and Infrared (IR) activities. A_{1g} (R), E_g, (R), and $3T_{2g}$ (R) [60] are the five first active modes observed in the Raman spectrum at room temperature. The indication A, E, T, and g signified single, double and triple-dimension depiction and regularity to center of inversion, correspondingly [61,62]. In the Raman analysis, a distinct peak associated with the orthorhombic configuration of LaFeO₃

was not particularly prominent. However, there were minor peaks detected within the 550–750 cm^{-1} range, which were attributed to the presence of LaFeO₃ [63].

Following is the explanation based on the quasi-molecular depictions of soft ferrites which is associated to the regular mode movements of the tetrahedron (FeO₄): The A_{1g} (1) is attributed to Fe-O tetrahedral bonds stretching vibrations [40] appeared at 636.75–668.36 cm^{-1}, E_g and T_{2g} (3), existing in the ranges of 327.11–395.89 cm^{-1} and 472.23–530.45 cm^{-1} are assigned to symmetric and asymmetric bending of oxygen relative to Fe, respectively. T_{2g} (2) is associated to asymmetric stretching of Fe-O bond at 388.15–479.39 cm^{-1} and T_{2g} (1) translational movement of entire FeO₄ at 236.19–335.29 cm^{-1} as seen in Table 9. Same kinds of stretching vibrations were observed by M. I.
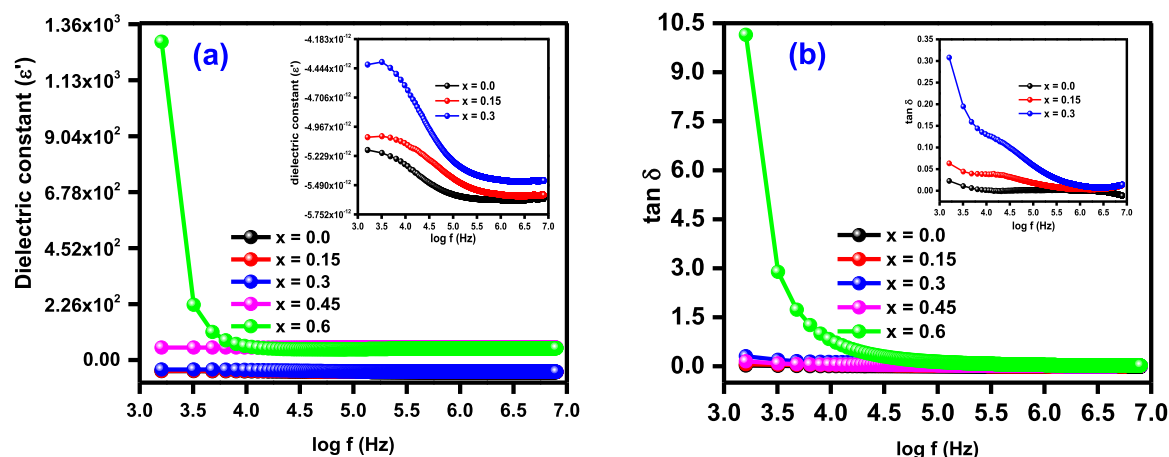
Fig. 12. (a-b): Plots of (a) Dielectric constant versus log of frequency (b) Dispersive loss versus log of frequency forMg^{2+} doped ZCLnano ferritesnano ferrites.
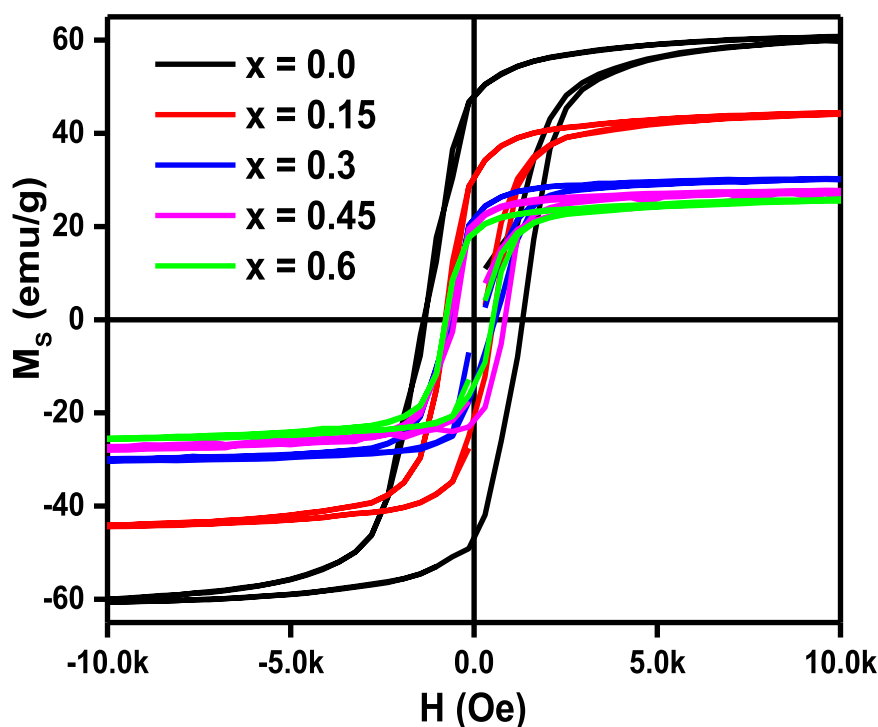
Fig. 13. Room temperature *M-H* loop for Mg^{2+} doped ZCLnano ferrites.

Table 11

Coercivity (H_C), Remnant squareness (SQ), Remanance (M_r), Saturation magnetization (M_s), Magnetic moment (n_B), Anisotropy constant (K), Initial permeability (μ_i), Y-K angle (α_{y-k}) and Microwave frequency (ω_m) for Mg^{2+} doped ZCL nano ferrites.

x	H_C (Oe)	M_r (emu/g)	M_s (emu/g)	SQ	K (erg/cm^3)	μ_i	n_B (μ_B)	ω_m (GHz)	H_m (Oe)	$\chi = dM/dH \times 10^{-3}$ (emu/g Oe)	
										$H \to 0$	$H \to H_m$
0.00	1334	47.82	60.82	0.7862	84,514.45	1.2968	0.49	13.4	1632.28	17.91	45.78
0.15	629	30.34	44.51	0.6816	29,163.32	1.7968	0.36	9.8	938.71	26.54	44.23
0.30	575	21.59	30.31	0.7123	18,154.42	1.2590	0.24	6.6	831.09	22.28	33.74
0.45	530	20.56	27.78	0.7401	15,336.87	1.4008	0.22	6.1	738.25	16.05	31.23
0.60	511	18.64	25.94	0.7185	13,807.64	1.9108	0.20	5.7	711.51	13.38	29.84

Arshad *et al.* [64]. The Raman spectra of Mg^{2+} substituted ferrites and five Raman active modes revealed in Fig. 7. The existence of different parameters in crystal structure like lattice deformation, the dislocation and contaminations are responsible for the observed vibrational band modes. Apart from the XRD results showing a single-phase nano ferrites, the occurrence of the peaks in Raman spectra can be illustrated as additional assurance of crystal field distortions. In the crystal field because of the transformations in polarizability in the course of
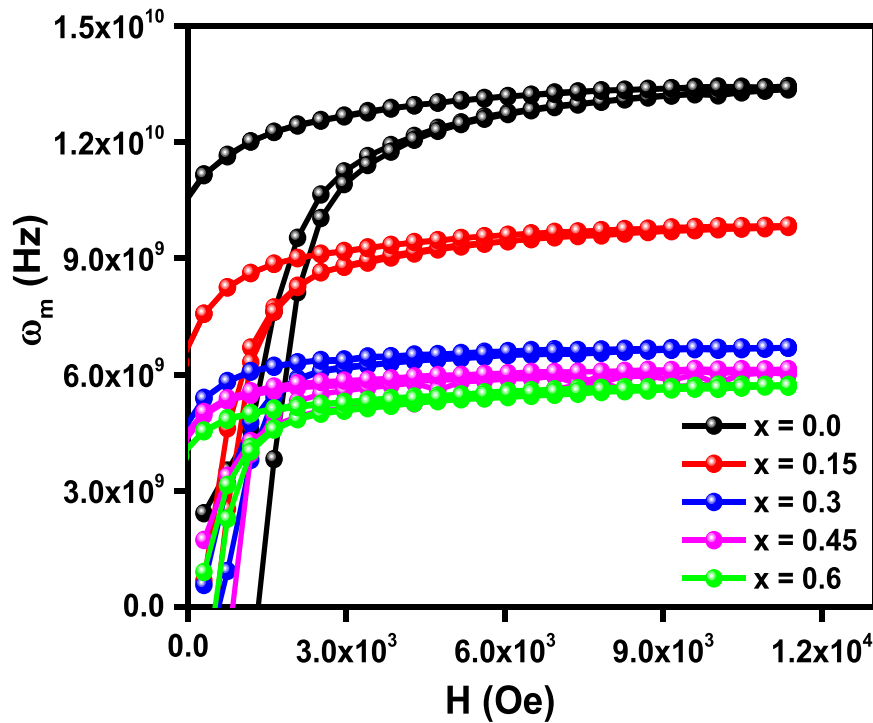
Fig. 14. Applied field vs. microwaves operating frequency for Mg^{2+} doped ZCLnano ferrites.

molecular vibration, the Raman active modes appear and depend upon failure of symmetry and Raman modes [62,65].

3.5. Electrical study

Fig. 8(a-b) shows the plots of electrical resistivity ($log\ \rho$) versus temperature (T) and the inverse of temperature ($10^3/T$). Fig. 8(a) indicates the relationship between the log of resistivity and temperature. The plots are divided into two ferromagnetic and paramagnetic region. It can be seen that resistivity of as-prepared samples increases with increasing temperature up to transition Curie (Tc) temperature. The results indicate the semiconductor behavior of Mg^{2+} doped ZCL. Except from the hopping of electrons amongst the cations of similar elements with the valency greater than 1 distributed over the lattice site describe the conduction process in soft nano ferrites instead of energy band theory [66]. The Curie temperature (T_C) reduces with Mg^{2+} doping (Table 10). Fig. 8(b) demonstrates the Arrhenius plots from which the activation energy (ΔE, $[\rho = \rho_0 e^{\frac{\Delta E}{K_B T}}]$ is calculated. The ΔE of paramagnetic (E_p) is higher than the ferromagnetic region (E_f). It is because paramagnetic are disordered states, while ferromagnetic are ordered states [67]. In paramagnetic states, charge carriers need enormous energy to move compared to those in the ferromagnetic states. Activation energies ($\Delta E = E_p - E_f$) decreased with dopant concentration (Fig. 9(b)), and the outcomes are reported in Table 10. Fig. 9(a) represents the relationship amongst the ferromagnetic and paramagnetic region and resistivity decreases with the increase of Mg^{2+} doping. DC resistivity is inversely associated to drift mobility (μ_d) [68]. Fig. 10 shows drift mobility (μ_d) versus temperature. The values for "μ_d" increased with increasing temperature. This fact implies that the "μ_d" of charge carriers (thermally generated) enhances with increased temperature (T). It can be observed (Fig. 9(b)) that μ_d increases with dopant and the values of 323 K are given in Table 10.

3.6. UV–vis spectroscopy study

The optical bandgap energy (E_g) of nano-ferrites usually associated

to grain size, impurities, lattice strain, lattice parameters, surfacial contact, and the concentration of dopant ions [69]. Fig. 11 shows Tauc plots [70] by employing the UV–vis photometer. The "E_g" was determined and its values are plotted in Fig. 11. The "E_g" reduces from 2.61 eV to 1.47 eV, as the concentration of Mg^{2+} increased. When nanoparticle structures are formed due to changes in composition, quantum confinement effects can occur. Smaller particle sizes can result in quantization of energy levels which can lead to a lower band gap of ZCL ferrites. It can be observed that optical band gap energy decreases significantly with the addition of Mg^{2+} concentration due to the quantum confinement effect [71]. The other E_g' values are also appearing in the inner sides of the Tauc's plots for $x = 0.0$–0.6 as shown in Fig. 11 and associated results are 2.89 eV, 2.64 eV, 2.34 eV, 2.21 eV and 1.90 eV. The decrease in optical band gap energy was also observed by M. S. Hasan *et al.* to confirm the semiconducting nature of ferrites [38]. In addition, the alteration of cationic species (Mg and Co) in the lattice can influence charge transfer between ions. This charge transfer can affect the energy levels of electrons and holes within the material, leading to a change in the band gap.

3.7. Dielectric properties

At 300 K, the dielectric constant (ε') of Mg^{2+} doped *ZCL nano-ferrites* versus frequency was measured within the 8 Hz to 8 MHz frequency range and the data are given in Fig. 12(a). The dielectric constant (ε') showed reducing trend with the increasing frequency and become constant at large frequency. Such trend is due to space charge polarization because of inhomogeneous structures of nanoparticles. This sort of nano ferrites dielectric behavior accredited to Maxwell-Wagner interfacial polarization in concurrence with Koop's phenomenological theory [72] in which the nano-ferrites act as a multilayer capacitor consisting of grains and grain boundaries. Moreover, the defects in nano-ferrites responsible for poor conductive grain boundaries in lower frequency, whereas in greater frequency, smooth grains are more effective due to high conductivity. The reduction in "ε'" values at high frequency is associated to interior grains because the charge carrier
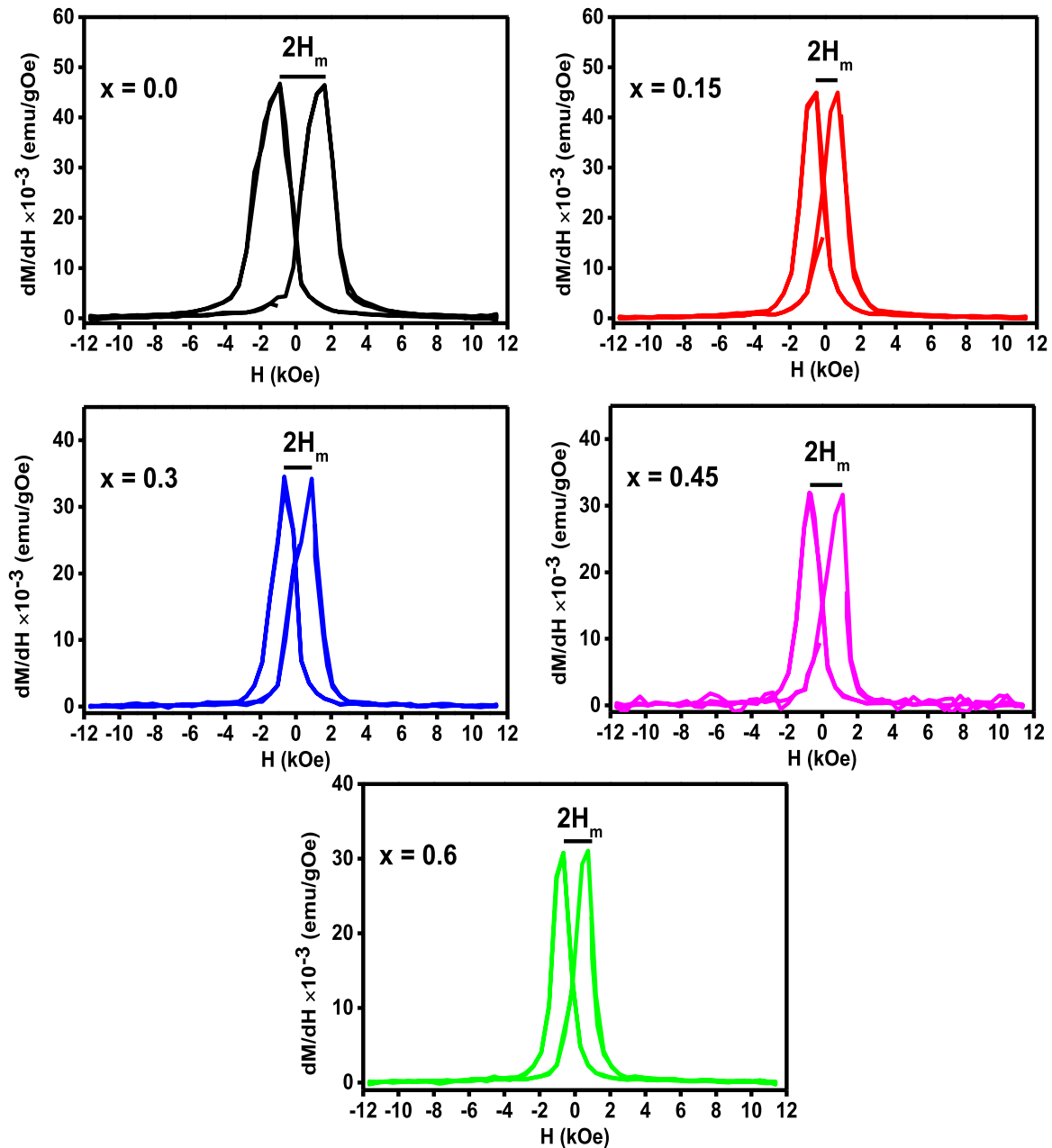
Fig. 15. Field dependence cure for Mg^{2+} doped ZCL nano ferrites.

hopping do not follow the applied field [73]. In Mg^{2+} inserted ZCL nano-ferrites, the conduction sources including $Fe^{3+}— O^{2-}—$ Me (Me is Mg^{2+}, Zn^{2+}, Co^{2+} and La^{3+}) and $Fe^{3+}— O^{2-}— Fe^{3+}$ are basis for hopping and it plays a significant role in the conduction mechanism.

At 300 K, the plot of dispersive loss ($tan\delta$) and frequency is given in Fig. 12(b). The dispersive (tangent) loss demonstrates same trends for dielectric constant with an increasing frequency. At low frequency, the dispersive (tangent) loss has greater values for the as-prepared nano ferrites. It may be due to the crystal defects attributed to the domination of exceedingly resistive grain boundaries. At higher frequency dispersive (tangent) loss is larger due to low resistive grains [74]. The declination in both dielectric factors were also observed by Maria *et al.* in Mg doped Co-Zn ferrites [23].

3.8. VSM analysis

M-H loops for Mg^{2+} substituted *ZCL nano-ferrites* are shown in

Fig. 13. The measured coercivity (H_c), remnant magnetization (M_r), saturation magnetization (M_S) and squareness ratio ($SQ =M_r/M_S$) from *M-H* loops are listed in Table 11. It can be seen that M_S decreases with the addition of Mg^{2+} concentration which can be attributed to cations distributions. The addition of Mg^{2+} leads to a reduction in the saturation magnetization and remanence magnetization. In a ferromagnetic spinel structure, the magnetic ordering arises from super-exchange interactions between metal ions in the A and B sub-lattices. The decrease in saturation magnetization is attributed to the incorporation of iron into the A site giving rise to the diminishing strength of the exchange interaction between A and B sites. Furthermore, $CoFe_2O_4$ exhibits a mixed spinel structure featuring a non-collinear ferromagnetic spin arrangement, with crystallite sizes ranging from 20 to 10 nm. The reduction in saturation magnetization can also be attributed to the presence of this non-collinear spin configuration on the particle surfaces [75]. Also it may also attributed to the introduction Zn^{2+} in ZCL ferrites leads the decrease in A-B interactions and increase in B-B interactions

[76]. In our work maximum *Ms* of 60.82 emu/g is observed which is higher than 42.29 mu/g found in Mg doped CoZn ferrites by Kaur *et al.* [77]. While, in current research work maximum $Ms = 60.82$ emu/g is observed. The coercivity (H_c) are ranging from 511 Oe to 1134 Oe and it decreases with the increase of Mg^{2+} concentration. M_r and M_S indicated the same behavior as coercivity (H_c). The squareness ratio indicates how square the hysteresis loop is [78]. Coercivity (Hc) is the magnetic field strength required to demagnetize the material. It is determined by examining the M-H loop during the decreasing field phase. As we reduce the applied field from its positive maximum, the magnetization will start decreasing. The coercivity is reached when the magnetization drops to zero or crosses a predefined threshold value in the negative direction. N. Tomas *et al.* also found the decrease in H_c in the range of 930 – 89 Oe with the addition of Mg^{2+} concentration [16]. In H_c is also decreasing with the increase of Mg^{2+} concentration as given in Table 11. H_c is associated to magnetocrystalline anisotropy and size of nanoparticles in ZCL ferrites. Hence, the reduction in values of Hc are attributed to magnetocrystalline anisotropy of ZCL ferrites due to the insertion of Mg^{2+} ions [71]. The decrease in anisotropy field is attributed to reduction in energy of domain walls [15].

The squareness ratio *SQ* decreased from 0.78 to 0.51 as concentration of Mg^{2+} increased from 0.0 to 0.6 and the calculated *SQ* being less than one, indicating the superparamagnetic behavior of Mg^{2+} substituted ZCL spinel ferrites [79]. Tulu Wegayehu Mammo *et al.* also investigated the reduction in magnetic parameters with increase of magnesium contents [15].

The anisotropy constant ($K = H_C \times M_S/0.96$) and initial permeability ($\mu_i = M_S^2 \times D/K$) were also reported in Table 11. The addition of Mg^{2+} cations led to a decrease in the "K" value, and the lowest initial permeability was observed at x = 0.3. Typically, "K" is impacted by crystallographic orientations, crystalline anisotropy, and particle size. When particle size increases "K" values decrease and domain walls are formed. In such instances, the dominant contribution to magnetization arises from the movement of domain walls rather than domain rotation. In the current research, the reduction in "K" values is ascribed to the presence of dopant ions [80].

Soft ferrites have significant microwave applications and the equation $\omega_m = 8\pi^2 M_s \gamma$ can be used to investigate the high-frequency (where, $\gamma = 2.8$ MHz/Oe is the gyromagnetic ratio) [26,81]. Fig. 14 shows the response of "ω_m" for Mg^{2+} substituted ZCL nano ferrites from which it can be seen that the ferrites could be used for high-frequency strategies. At the same time, the current magnetic materials were capable to be functioned in microwave frequency range 13.4 – 5.7 GHz.

In order to justify the aspects of single domain (SD)/pseudo-single domain (PSD) and multi-domain (MD) behavior over RT, the field dependence of magnetization was measured and the data of dM/dH [82] which is identified as the magnetic susceptibility (χ) curve are shown in Fig. 15. For ideal domain ferrites consist of *M–H* square curve where coercivity (H_C) is zero as $H \to 0$, $\chi = dM/dH$ has an important role. $\chi = dM/dH$ at $H \to 0$ with limited values verifying the features of *SD/PSD* and *MD* grains in synthesized Mg^{2+} doped ZCL ferrites as given in Table 11. Fig. 15 signifies the *dM/dH* against *H* curve specifying the peak at $\sim H_m$ and being split by $2H_m$ and symmetric about $H \to 0$. Table 11 shows the results at $H \to H_m$ of H_m and dM/dH. H_m has higher values than the H_C and it signifies the switching field distribution (SFD) due to disordered shell arrangements in PSD and MD grains [83]. At H_m the "χ" for peak heights are also illustrated in Table 11 and exposed the higher outcomes of "χ" at $H \to H_m$ than the values at $H \to 0$. At *Hm* the enhancement in both peak partitions and peak heights of "χ" leads to the stability and good crystallization cubic matrix of ferrites. While, the opposite behavior of peaks makes the nano-ferrites extremely unstable superparamagnetic domains [84].

4. Conclusion

Mg substituted $Zn_{0.4}Co_{0.6-x}Mg_xFe_{1.9}La_{0.1}O_4$ soft ferrites (x = 0.00, 0.15, 0.30, 0.45, 0.60) were prepared by co-precipitation route. The average crystallite size and lattice constant revealed reducing behavior for x = 0.0 – 0.45 with maximum value at x = 0.60. Different parameters were calculated by the application of XRD data. The morphological analysis verified the agglomerated form of nanoparticles. Optical bandgap energy decreased from 2.61 eV to 1.47 eV and an additional optical band gap was also observed. DC electrical resistivity expressed opposed behavior in paramagnetic and ferromagnetic regions. The Curie temperature decreased with the growth of magnesium contents. Tetrahedral and octahedral bands were detected in the range of 550.96 cm^{-1} – 552.39 cm^{-1} and 413.57 cm^{-1} – 403.56 cm^{-1} respectively, in FTIR spectra. Five active phonon modes were identified ($\Gamma = 1A_{1\,g} + 1E_g + 3\,T_{2\,g}$) for regular spinel structure. Dielectric constant and dielectric loss exposed reducing trends with the increasing frequency. The magnetic parameters (M_r, M_s and H_c) declined with the addition of magnesium contents. The frequency range (13.4 – 5.7 GHz) was determined by using saturation magnetization and exposed that Mg^{2+} doped ZCL particles are favorite candidates for high-frequency devices.

CRediT authorship contribution statement

M.I. Arshad: Conceived the idea, Supervision, Project administration. **M.S. Hasan:** Writing – original draft. **Atta Ur Rehman**: Methodology, writing, editing. **N. Amin**: Validation of data. **Le Duc Tung**: Review. **Nguyen Thi Kim Thanh**: Data analysis, critical review. **N.A. Morley**: Review. **Faisal Alresheedi**: Data analysis. **Safa Ezzine:**Resources. **M. A. Gadhi**: Data analysis. All authors discussed the results and commented on the manuscript.

Declaration of Competing Interest

The authors declare that they have no known competing financial interests or personal relationships that could have appeared to influence the work reported in this paper.

Data availability

Data will be made available on request.

References

[1] M. Hashim, S. Meena, R. Kotnala, S.E. Shirsath, P. Bhatt, S. Kumar, E. Şentürk, R. Kumar, N. Gupta, Exploring the structural, Mössbauer and dielectric properties of Co2+ incorporated Mg0. 5Zn0. 5− xCoxFe2O4 nanocrystalline ferrite, J. Magn. Magn. Mater. 360 (2014) 21–33.

[2] M. Abdellatif, A. Azab, M. Salerno, Effect of rare earth doping on the vibrational spectra of spinel Mn-Cr ferrite, Mater. Res. Bull. 97 (2018) 260–264.

[3] R. Valenzuela, Novel applications of ferrites, Phys. Res. Int. (2012) (2012).

[4] K.K. Kefeni, T.A. Msagati, T.T. Nkambule, B.B. Mamba, Spinel ferrite nanoparticles and nanocomposites for biomedical applications and their toxicity, Mater. Sci. Eng. C 107 (2020), 110314.

[5] S. Zhang, X. Liu, L. Zhou, W.J.M.L. Peng, Magnetite nanostructures: one-pot synthesis, superparamagnetic property and application in magnetic resonance imaging, 68, 2012: 243–246.

[6] M. Banerjee, A. Mukherjee, S. Chakrabarty, S. Basu, M. Pal, Bismuth-Doped Nickel Ferrite Nanoparticles for Room Temperature Memory Devices, ACS Appl. Nano Mater. 2 (2019) 7795–7802.

[7] S. Goel, M. Bala, A. Garg, V.D. Shivling, S. Tyagi, Lanthanum doped barium hexaferrite nanoparticles for enhanced microwave absorption, Materials Today: Proceedings 28 (3) (2020) 1753–1758.

[8] K. Mohit, V.R. Gupta, N. Gupta, S.J.C.I. Rout, Structural and microwave characterization of Ni0. 2CoxZn0. 8− xFe2O4 for antenna applications, 40, 2014: 1575–1586.

[9] R. Jasrotia, V.P. Singh, B. Sharma, A. Verma, P. Puri, R. Sharma, M.J.Jo.A. Singh, Compd., Sol. -gel Synth. Ba-Nd-Cd- nanohexaferrites High. Freq. Microw. Devices Appl. (2020), 154687.

[10] A. Nigam, S.J.C.I. Pawar, Structural, magnetic, and antimicrobial properties of zinc doped magnesium ferrite for drug delivery applications, 46, 2020: 4058–4064.

[11] K. Srinivasamurthy, S. Kubrin, S. Matteppanavar, D. Sarychev, P.M. Kumar, H.W. Azale, B.J.C.I. Rudraswamy, Tuning of ferrimagnetic nature and hyperfine interaction of Ni2+ doped cobalt ferrite nanoparticles for power transformer applications, 44, 2018: 9194–9203.

[12] K. Ukoba, A. Eloka-Eboka, F. Inambao, Review of nanostructured NiO thin film deposition using the spray pyrolysis technique, Renew. Sustain. Energy Rev. 82 (2018) 2900–2915.

[13] S. Giri, S. Samanta, S. Maji, S. Ganguli, A. Bhaumik, Magnetic properties of α-Fe2O3 nanoparticle synthesized by a new hydrothermal method, J. Magn. Magn. Mater. 285 (2005) 296–302.

[14] P. Singjai, K. Wongwigkarn, Y. Laosiritaworn, R. Yimnirun, S. Maensiri, Carbon encapsulated nickel nanoparticles synthesized by a modified alcohol catalytic chemical vapor deposition method, Curr. Appl. Phys. 7 (2007) 662–666.

[15] T.W. Mammo, N. Murali, Y.M. Sileshi, T. Arunamani, Studies of structural, morphological, electrical, and magnetic properties of Mg-substituted Co-ferrite materials synthesized using sol-gel autocombustion method, Phys. B: Condens. Matter 523 (2017) 24–30.

[16] N. Thomas, P. Jithin, V. Sudheesh, V. Sebastian, Magnetic and dielectric properties of magnesium substituted cobalt ferrite samples synthesized via one step calcination free solution combustion method, Ceram. Int. 43 (2017) 7305–7310.

[17] M. Hasan, M. Arshad, A. Ali, K. Mahmood, N. Amin, S. Ali, M. Khan, G. Mustafa, M. Khan, M. Saleem, Mg and La co-doped ZnNi spinel ferrites for low resistive applications, Mater. Res. Express 6 (2018), 016302.

[18] N. Amin, R. Bilal, G. Mustafa, A. Aslam, M. Hasan, K. Hussain, M. Tabassum, M. Fatima, Z. Khan, A. Naseem, IMPACTS OF SUBSTITUTING Ni 2 IONS ON STRUCTURAL AND ELECTRICAL PROPERTIES OF W-TYPE BARIUM BASED HEXAFERRITES, Dig. J. NANOMATERIALS BIOSTRUCTURES 14 (2019) 501–507.

[19] T. Dippong, E.A. Levei, G. Borodi, F. Goga, L. Barbu, Tudoran, Influence of Co/Fe ratio on the oxide phases in nanoparticles of Co x Fe 3− x O 4, J. Therm. Anal. Calorim. 119 (2015) 1001–1009.

[20] T. Dippong, E.A. Levei, O. Cadar, Investigation of structural, morphological and magnetic properties of MFe2O4 (M= Co, Ni, Zn, Cu, Mn) obtained by thermal decomposition, Int. J. Mol. Sci. 23 (2022) 8483.

[21] T. Dippong, E.A. Levei, O. Cadar, I.G. Deac, M. Lazar, G. Borodi, I. Petean, Effect of amorphous SiO2 matrix on structural and magnetic properties of Cu0. 6Co0. 4Fe2O4/SiO2 nanocomposites, J. Alloy. Compd. 849 (2020), 156695.

[22] S. Bhukal, R. Sharma, S. Mor, S. Singhal, Mg–Co–Zn magnetic nanoferrites: characterization and their use for remediation of textile wastewater, Superlattices Microstruct. 77 (2015) 134–151.

[23] M.Y. Lodhi, K. Mahmood, A. Mahmood, H. Malik, M.F. Warsi, I. Shakir, M. Asghar, M.A. Khan, New Mg0. 5CoxZn0. 5− xFe2O4 nano-ferrites: structural elucidation and electromagnetic behavior evaluation, Curr. Appl. Phys. 14 (2014) 716–720.

[24] M.A. Rafiq, M.A. Khan, M. Asghar, S. Ilyas, I. Shakir, M. Shahid, M.F. Warsi, Influence of Co2+ on structural and electromagnetic properties of Mg–Zn nanocrystals synthesized via co-precipitation route, Ceram. Int. 41 (2015) 10501–10505.

[25] Y. Liu, S. Wei, Y. Wang, H. Tian, H. Tong, B. Xu, Characterization of (Mg, La) Substituted Ni-Zn Spinel Ferrite, Phys. Procedia 50 (2013) 43–47.

[26] S. Gaba, A. Kumar, P.S. Rana, M. Arora, Influence of La3+ ion doping on physical properties of magnesium nanoferrites for microwave absorption application, J. Magn. Magn. Mater. 460 (2018) 69–77.

[27] T. Dippong, E.A. Levei, O. Cadar, A. Mesaros, G. Borodi, Sol-gel synthesis of CoFe2O4: SiO2 nanocomposites–insights into the thermal decomposition process of precursors, J. Anal. Appl. Pyrolysis 125 (2017) 169–177.

[28] P. Barvinschi, O. Stefanescu, T. Dippong, S. Sorescu, M. Stefanescu, CoFe 2 O 4/SiO 2 nanocomposites by thermal decomposition of some complex combinations embedded in hybrid silica gels, J. Therm. Anal. Calorim. 112 (2013) 447–453.

[29] T. Dippong, E.-A. Levei, D. Toloman, L. Barbu-Tudoran, O. Cadar, Investigation on the formation, structural and photocatalytic properties of mixed Mn-Zn ferrites nanoparticles embedded in SiO2 matrix, J. Anal. Appl. Pyrolysis 158 (2021), 105281.

[30] M. Bhandare, H. Jamadar, A. Pathan, B. Chougule, A.J.Joa Shaikh, compounds, Dielectric properties of Cu substituted Ni0. 5− xZn0. 3Mg0. 2Fe2O4 ferrites, 509, 2011: L113-L118.

[31] R.R. Kanna, N. Lenin, K. Sakthipandi, M.J.C.I. Sivabharathy, Impact of lanthanum on structural, optical, dielectric and magnetic properties of Mn1-xCuxFe1. 85La0. 15O4 spinel nanoferrites, 43, 2017: 15868–15879.

[32] M.I.A. Abdel Maksoud, A. El-Ghandour, A.H. Ashour, M.M. Atta, S. Abdelhaleem, A.H. El-Hanbaly, R.A. Fahim, S.M. Kassem, M.S. Shalaby, A.S. Awed, La³⁺ doped LiCo$_{0.25}$Zn$_{0.25}$Fe$_2$O$_4$ spinel ferrite nanocrystals: Insights on structural, optical and magnetic properties, J. Rare Earths. 39 (1) (2021) 75–82.

[33] S. Raghuvanshi, P. Tiwari, S.N. Kane, D.K. Avasthi, F. Mazaleyrat, T. Tatarchuk, I. Mironyuk, Dual control on structure and magnetic properties of Mg ferrite: role of swift heavy ion irradiation, Journal of Magnetism and Magnetic Materials 471 (2019) 521–528.

[34] V. Mameli, A. Musinu, A. Ardu, G. Ennas, D. Peddis, D. Niznansky, Nguyen T. K. Thanh, C. Cannas, Studying the effect of Zn-substitution on the magnetic and hyperthermic properties of cobalt ferrite nanoparticles, Nanoscale 8 (19) (2016) 10124–10137.

[35] M. Hasan, S. Ali, M. Rizwan, M. Khan, H.N. Ullah, M.I. Irfan, Structural, Optical, Electrical and Magnetic Properties of Cu0. 2Zn0. 2Ni0. 6-xMgxFe2O4 (x= 0.00, 0.15, 0.30, 0.45, 0.60) Soft Ferrites, J. Alloy. Compd. (2023), 170392.

[36] M. Nabi, M. Moin, M. Hasan, M. Arshad, A. Bibi, N. Amin, K. Mahmood, S. Ali, Study of electrical Transport properties of cadmium-doped Zn−Mn soft ferrites by Co-precipitation method, J. Supercond. Nov. Magn. 34 (2021) 1813–1822.

[37] S. Anand, A.P. Amaliya, M.A. Janifer, S.J.M.E.M. Pauline, Structural, morphological and dielectric studies of zirconium substituted CoFe2O4 nanoparticles, 3, 2017: 168–173.

[38] M. Hasan, S. Ali, M. Khan, M. Rizwan, M. Zulqarnain, A. Hussain, Structural, optical, electrical and magnetic tuning based on Zn substitution at A site in yttrium doped spinel ferrites, Mater. Chem. Phys. 301 (2023), 127538.

[39] W.A. Farooq, M. Sajjad Ul Hasan, M.I. Khan, A.R. Ashraf, M. Abdul Qayyum, N. Yaqub, M.A. Almutairi, M. Atif, A. Hanif, Structural, Optical and Electrical Properties of Cu0. 6CoxZn0. 4− xFe2O4 (x= 0.0, 0.1, 0.2, 0.3, 0.4) Soft Ferrites, Molecules 26 (2021) 1399.

[40] M. Akhtar, M. Hasan, N. Amin, N. Morley, M.I. Arshad, Tuning structural, electrical, dielectric and magnetic properties of Mg–Cu–Co ferrites via dysprosium (Dy3+) doping, Journal of Rare Earths, (2023).

[41] N. Amin, M.S.U. Hasan, Z. Majeed, Z. Latif, M.A. un Nabi, K. Mahmood, A. Ali, K. Mehmood, M. Fatima, M.J.C.I. Akhtar, Structural, electrical, optical and dielectric properties of yttrium substituted cadmium ferrites prepared by Co-Precipitation method, (2020).

[42] M. Khan, G. Hassan, M. Hasan, S.A. Abubshait, H.A. Abubshait, W. Al-Masry, Q. Mahmood, A. Mahmood, S.M. Ramay, Investigations on the efficiency variation of zinc and gallium Co-doped TiO2 based dye sensitized solar cells, Ceram. Int. 46 (2020) 24844–24849.

[43] A. Mujtaba, M. Khan, M. Hasan, S. Ali, W. Shahid, M. Fatima, H.S. Abd-Rabboh, N. Alwadai, Tailoring the structural, optical, photoluminescence, dielectric and electrical properties of Zn0·6Ni0·2Mg0·2Fe2-xLaxO4 (x= 0.00, 0.0125, 0.0250, 0.0375), J. Mater. Res. Technol. 23 (2023) 4538–4550.

[44] V. Chaudhari, S.E. Shirsath, M. Mane, R. Kadam, S. Shelke, D. Mane, Crystallographic, magnetic and electrical properties of Ni0. 5Cu0. 25Zn0. 25LaxFe2− xO4 nanoparticles fabricated by sol–gel method, J. Alloy. Compd. 549 (2013) 213–220.

[45] M. Saqib, S. Ali, M. Zulqarnain, M.U. Qadri, M. Riaz, M. Hasan, M. Khan, M. Tahir, M. Arshad, H. Rani, Temperature-dependent variations in structural, magnetic, and optical behavior of doped ferrites nanoparticles, J. Supercond. Nov. Magn. 34 (2021) 609–616.

[46] M.N. Akhtar, M.A. Khan, Effect of rare earth doping on the structural and magnetic features of nanocrystalline spinel ferrites prepared via sol gel route, J. Magn. Magn. Mater. 460 (2018) 268–277.

[47] I. Ahmad, T. Abbas, M. Islam, A. Maqsood, Study of cation distribution for Cu–Co nanoferrites synthesized by the sol–gel method, Ceram. Int. 39 (2013) 6735–6741.

[48] K.M. Batoo, G. Kumar, Y. Yang, Y. Al-Douri, M. Singh, R.B. Jotania, A. Imran, Structural, morphological and electrical properties of Cd2+ doped MgFe2-xO4 ferrite nanoparticles, J. Alloy. Compd. 726 (2017) 179–186.

[49] M. Zulqarnain, S. Ali, U. Hira, J. Feng, M. Khan, M. Rizwan, K. Javed, G. Farid, M. Hasan, Superparamagnetic contributions, optical band gap tuning and dominant interfacial resistive mechanisms in ferrites nanostructures, J. Alloy. Compd. 894 (2022), 162431.

[50] A. Goldman, Modern ferrite technology, Springer Science & Business Media,, 2006.

[51] R. Sharma, S. Singhal, Structural, magnetic and electrical properties of zinc doped nickel ferrite and their application in photo catalytic degradation of methylene blue, Phys. B: Condens. Matter 414 (2013) 83–90.

[52] R. Sharma, P. Thakur, P. Sharma, V. Sharma, Ferrimagnetic Ni2+ doped Mg-Zn spinel ferrite nanoparticles for high density information storage, J. Alloy. Compd. 704 (2017) 7–17.

[53] P. Thakur, R. Sharma, M. Kumar, S. Katyal, N. Negi, N. Thakur, V. Sharma, P. Sharma, Superparamagnetic La doped Mn–Zn nano ferrites: dependence on dopant content and crystallite size, Mater. Res. Express 3 (2016), 075001.

[54] M. Khan, M. Waqas, M. Naeem, M. Hasan, M. Iqbal, A. Mahmood, S.M. Ramay, W. Al-Masry, S.A. Abubshait, H.A. Abubshait, Magnetic behavior of Ga doped yttrium iron garnet ferrite thin films deposited by sol-gel technique, Ceram. Int. 46 (2020) 27318–27325.

[55] M. NABI, M. Sharif, G. Mustafa, A. ALIa, K. Mahmood, N. ALIc, N. Amin, M. Ahmad, N. Sabir, M. Asif, STRUCTURAL AND THERMOELECTRIC POWER STUDIES OF Sm 3-SUBSTITUTED Li-Ni-SPINEL FERRITE, Dig. J. NANOMATERIALS BIOSTRUCTURES 13 (2018) 1111–1116.

[56] M. Hasan, M. Khan, S. Kanwal, M. Irfan, T.I. Al-Muhimeed, S. Mumtaz, Structural, optical and electrical impacts of Ni 2+ on Fe 1.9 Sm 0.1 O 4 (x= 0.0, 0.2, 0.4 and 0.6) spinel ferrites, Dig. J. Nanomater. Biostructures (DJNB) 17 (2022).

[57] S. Yasmeen, F. Iqbal, T. Munawar, M.A. Nawaz, M. Asghar, A.J.C.I. Hussain, Synthesis, structural and optical analysis of surfactant assisted ZnO–NiO nanocomposites prepared by homogeneous precipitation method, 45, 2019: 17859–17873.

[58] M.M.L. Sonia, S. Anand, V.M. Vinosel, et al., Effect of lattice strain on structural, magnetic and dielectric properties of sol–gel synthesized nanocrystalline Ce^{3+} substituted nickel ferrite, J Mater Sci: Mater Electron 29 (2018) 15006–15021.

[59] R. Gupta, A. Sood, P. Metcalf, J. Honig, Raman study of stoichiometric and Zn-doped Fe 3 O 4, Phys. Rev. B 65 (2002), 104430.

[60] M.A.U. Nabi, M. Moin, M. Hasan, M. Arshad, A. Bibi, N. Amin, K. Mahmood, S. Ali, Study of electrical transport properties of cadmium-doped Zn–Mn soft ferrites by co-precipitation method, J. Supercond. Nov. Magn. 34 (2021) 1813–1822.

[61] R. Waldron, Infrared spectra of ferrites, Phys. Rev. 99 (1955) 1727.

[62] P. Graves, C. Johnston, J. Campaniello, Raman scattering in spinel structure ferrites, Mater. Res. Bull. 23 (1988) 1651–1660.

[63] M. Popa, J. Frantti, M. Kakihana, Lanthanum ferrite LaFeO3+ d nanopowders obtained by the polymerizable complex method, Solid State Ion. 154 (2002) 437–445.

[64] M.I. Arshad, M. Hasan, A.U. Rehman, M. Akhtar, N. Amin, K. Mahmood, A. Ali, T. Trakoolwilaiwan, N.T.K. Thanh, Structural, optical, electrical, dielectric, molecular vibrational and magnetic properties of La3+ doped Mg–Cd–Cu ferrites prepared by Co-precipitation technique, Ceram. Int. 48 (2022) 14246–14260.

[65] M. Abdellatif, G. Abdelrasoul, M. Salerno, I. Liakos, A. Scarpellini, S. Marras, A. Diaspro, Fractal analysis of inter-particle interaction forces in gold nanoparticle aggregates, Colloids Surf. A: Physicochem. Eng. Asp. 497 (2016) 225–232.

[66] M. Raghasudha, D. Ravinder, P. Veerasomaiah, Electrical resistivity studies of Cr doped Mg nano-ferrites, Materials, Discovery 2 (2015) 50–54.

[67] R.G. Kharabe, R.S. Devan, B.K. Chougale, Structural and electrical properties of Cd-substituted Li–Ni ferrites, J. Alloy. Compd. 463 (2008) 67–72.

[68] K. Jalaiah, K.C. Mouli, R. Krishnaiah, K.V. Babu, P.S. Rao, The structural, DC resistivity and magnetic properties of Zr and Co co-substituted Ni0. 5Zn0. 5Fe2O4, Heliyon 5 (2019), e01800.

[69] A. Manikandan, L.J. Kennedy, M. Bououdina, J.J. Vijaya, Synthesis, optical and magnetic properties of pure and Co-doped ZnFe2O4 nanoparticles by microwave combustion method, J. Magn. Magn. Mater. 349 (2014) 249–258.

[70] K. Hussain, N. Amin, M. Ajaz-Un-Nabi, A. Ali, K. Mahmood, G. Mustafa, M. Sharif, M. Hasan, N. Sabir, S. Ali, Investigation of structural and electrical properties of Ce3+ ions substituted Cd-Co Ferrites, Dig. J. Nanomater. Biostruct. 14 (2019) 85–92.

[71] A.G. Abraham, A. Manikandan, E. Manikandan, S. Vadivel, S. Jaganathan, A. Baykal, P.S. Renganathan, Enhanced magneto-optical and photo-catalytic properties of transition metal cobalt (Co2+ ions) doped spinel MgFe2O4 ferrite nanocomposites, J. Magn. Magn. Mater. 452 (2018) 380–388.

[72] J.C. Maxwell, Electricity and magnetism, Dover, New York, 1954.

[73] Z. Ahmad, S. Atiq, S.K. Abbas, S.M. Ramay, S. Riaz, S.J.C.I. Naseem, Structural and complex impedance spectroscopic studies of Mg-substituted CoFe2O4, 42, 2016: 18271–18282.

[74] E. Melagiriyappa, H. Jayanna, B. Chougule, Dielectric behavior and ac electrical conductivity study of Sm3+ substituted Mg–Zn ferrites, Mater. Chem. Phys. 112 (2008) 68–73.

[75] H. Moradmard, S.F. Shayesteh, P. Tohidi, Z. Abbas, M. Khaleghi, Structural, magnetic and dielectric properties of magnesium doped nickel ferrite nanoparticles, J. Alloy. Compd. 650 (2015) 116–122.

[76] T. Dippong, I.G. Deac, O. Cadar, E.A. Levei, Effect of silica embedding on the structure, morphology and magnetic behavior of (Zn0. 6Mn0. 4Fe2O4) δ/(SiO2) (100− δ) nanoparticles, Nanomaterials 11 (2021) 2232.

[77] M. Kaur, P. Jain, M. Singh, Studies on structural and magnetic properties of ternary cobalt magnesium zinc (CMZ) Co0. 6-xMgxZn0. 4 Fe2O4 (x= 0.0, 0.2, 0.4, 0.6) ferrite nanoparticles, Mater. Chem. Phys. 162 (2015) 332–339.

[78] T. Dippong, E.A. Levei, I.G. Deac, I. Petean, O. Cadar, Dependence of structural, morphological and magnetic properties of manganese ferrite on Ni-Mn substitution, Int. J. Mol. Sci. 23 (2022) 3097.

[79] M.N. Akhtar, M.S. Nazir, Z. Tahir, S. Qamar, M.A. Khan, Impact of Co doping on physical, structural, microstructural and magnetic features of MgZn nanoferrites for high frequency applications, Ceramics International 46 (2) (2020) 1750–1759.

[80] T. Dippong, E.A. Levei, C. Leostean, O. Cadar, Impact of annealing temperature and ferrite content embedded in SiO2 matrix on the structure, morphology and magnetic characteristics of (Co0. 4Mn0. 6Fe2O4) δ (SiO2) 100-δ nanocomposites, J. Alloy. Compd. 868 (2021), 159203.

[81] A. Majeed, M.A. Khan, F. ur Raheem, A. Hussain, F. Iqbal, G. Murtaza, M.N. Akhtar, I. Shakir, M.F. Warsi, , Structural elucidation and magnetic behavior evaluation of rare earth (La, Nd, Gd, Tb, Dy) doped BaCoNi-X hexagonal nano-sized ferrites, J. Magn. Magn. Mater. 408 (2016) 147–151.

[82] I.P. Muthuselvam, R.N. Bhowmik, Structural phase stability and magnetism in Co2FeO4 spinel oxide, Solid State Sci. 11 (2009) 719–725.

[83] W. Zhang, A. Sun, X. Zhao, et al., Structural and magnetic properties of La^{3+} ion doped Ni–Cu–Co nano ferrites prepared by sol–gel auto-combustion method, J Sol-Gel Sci Technol 90 (2019) 599–610.

[84] I.P. Muthuselvam, R.J.Jo.M. Bhowmik, M. Materials, Mechanical alloyed Ho3+ doping in CoFe2O4 spinel ferrite and understanding of magnetic nanodomains, 322, 2010: 767–776.